Examining Outer Band Supercell Environments in Landfalling Tropical Cyclones Using Ground-Based Radar Analyses

A. ADDISON ALFORD,[a,b,e] BENJAMIN SCHENKEL,[b,a,e] SAMUEL HERNANDEZ,[c] JUN A. ZHANG,[d] MICHAEL I. BIGGERSTAFF,[e,b,f] EMILY BLUMENAUER,[e] THEA N. SANDMÆL,[b,a] AND SEAN M. WAUGH[a]

[a] *NOAA/OAR/National Severe Storms Laboratory, Norman, Oklahoma*
[b] *Cooperative Institute for Severe and High-Impact Weather Research and Operations, University of Oklahoma, Norman, Oklahoma*
[c] *Saint Louis University, Saint Louis, Missouri*
[d] *NOAA/AOML/Hurricane Research Division, Miami, Florida*
[e] *School of Meteorology, University of Oklahoma, Norman, Oklahoma*
[f] *Advanced Radar Research Center, University of Oklahoma, Norman, Oklahoma*

(Manuscript received 18 December 2023, in final form 11 June 2024, accepted 29 June 2024)

ABSTRACT: Supercells in landfalling tropical cyclones (TCs) often produce tornadoes within 50 km of the coastline. The prevalence of TC tornadoes near the coast is not explained by the synoptic environments of the TC, suggesting a mesoscale influence is likely. Past case studies point to thermodynamic contrasts between ocean and land or convergence along the coast as a possible mechanism for enhancing supercell mesocyclones and storm intensity. This study augments past work by examining the changes in the hurricane boundary layer over land in the context of vertical wind shear. Using ground-based single- and dual-Doppler radar analyses, we show that the reduction in the boundary layer wind results in an increase in vertical wind shear/storm-relative helicity inland of the coast. We also show that convergence along the coast may be impactful to supercells as they cross the coastal boundary. Finally, we briefly document the changes in mesocyclone vertical vorticity to assess how the environmental changes may impact individual supercells.

KEYWORDS: Hurricanes/typhoons; Supercells; Tornadoes; Radars/Radar observations

1. Introduction

Supercells in tropical cyclones (TCs) represent one of the most significant wind and water hazards in the outer rainband environments and pose a threat to both life and property (Rappaport 2014; Brauer et al. 2020). TC supercells can cause locally increased winds that can reach severe criteria in addition to tornadoes (Vescio et al. 1996; Edwards 2012). Accurate forecasting of TC supercell environments is generally not a function of the intensity of the TC itself; rather, TCs with broader outer wind fields often spawn the greatest number of tornadoes regardless of their intensity (McCaul 1991; Edwards 2012; Paredes et al. 2021). Understanding TC supercell environments requires a comprehensive view of the environmental buoyancy and total vertical wind shear (VWS) which can often be concentrated in the lowest 1 km (Novlan and Gray 1974; McCaul 1991) as well as the VWS associated with the background synoptic environment (Schenkel et al. 2020, 2021). While the key environmental characteristics (e.g., buoyancy and VWS) that often support TC supercells are known, the mesoscale changes (such as small zones of enhanced buoyancy and VWS as in McCaul et al. 2004) in the environmental characteristics surrounding TC supercells have been understudied due to a lack of robust observations.

TC supercell environments differ from traditional supercell environments (e.g., in the U.S. Great Plains). Buoyancy is often substantially weaker in TC supercell environments than Great Plains supercell environments and is often maximized in the lowest few kilometers altitude compared to ~10-km altitude in Great Plains environments (McCaul 1991). Buoyancy is not uniform in the TC environment, however. Local dry air intrusions in the outer band environments may locally enhance buoyancy through midlevel evaporative cooling or through the erosion of convection and associated enhancements in local surface heating (e.g., McCaul 1991; Curtis 2004; Baker et al. 2009; Schultz and Cecil 2009). In contrast to buoyancy, VWS and helicity are often of similar (or greater) magnitude in TC supercell environments compared to Great Plains environments, but typically concentrated in the low levels (Eastin and Link 2009; Green et al. 2011; Baker et al. 2009; Carroll-Smith et al. 2019; Schenkel et al. 2020). Likewise, the distribution of VWS is not uniform. Based on climatology studies, tornadoes in general form in the right-front quadrant of the TC relative to TC motion and/or down and to the right of the synoptic-scale VWS vector (Gentry 1983; Baker et al. 2009; Molinari and Vollaro 2010; Schenkel et al. 2021). Recent observational work also suggests that the decrease in VWS and increase in buoyancy as a function of radius from the TC center result in a favorable overlap in VWS–buoyancy space in the outer bands (or at least a portion thereof; Schenkel et al. 2020; Nowotarski et al. 2021; Paredes et al. 2021; Trier et al. 2023).

Although buoyancy and VWS are routinely measured via National Weather Service radiosondes, TC supercell environments and their heterogeneities are likely undersampled (McCaul et al. 2004; Edwards and Pietrycha 2006). Taking radiosonde observations in TCs can be quite difficult, causing TC supercell proximity soundings to be relatively sparse

Corresponding author: A. Addison Alford, addison.alford@noaa.gov

DOI: 10.1175/MWR-D-23-0287.1

(McCaul 1991; Edwards and Thompson 2012; Nowotarski et al. 2021). Many studies attempting to examine mesoscale environments (i.e., those not resolved by the standard radiosonde network) of TC supercells employ numerical modeling to characterize the storm-scale and mesoscale environments of TC supercells. For example, on the meso-β scale, Green et al. (2011) showed a boundary that was draped across the U.S. Gulf Coast and interacted with TC supercells in Hurricane Katrina (2005) by enhancing low-level VWS that subsequently led to mesocyclone intensification in some supercells. However, the role of baroclinicity in storm-scale processes (e.g., mesocyclone intensification) is less certain (McCaul and Weisman 1996, 2001) but has been shown to be integral to mesoscale processes in the outer rainbands (Eastin et al. 2012). More generally, the coastal interface itself is hypothesized to lead to changes in the local supercell environment in TCs and can be influenced by the strength of the TC winds (Chen and Chavas 2020; Hlywiak and Nolan 2021). For example, in an observational study employing ground-based Weather Surveillance Radar-1988 Doppler (WSR-88D) and airborne radar analyses, supercells in Hurricane Ivan (2004) were observed to intensify as they moved onshore (Eastin and Link 2009). As the low-level, coast-perpendicular wind field responds to the increased surface roughness over land, some studies have suggested convergence along the coast may enhance updrafts, which would act to enhance tilting and stretching of low-level horizontal vorticity (Gentry 1983; Eastin and Link 2009; Green et al. 2011). Such a conceptual model is consistent with the near-coast tornado maximum (Gentry 1983; Schultz and Cecil 2009). Alternatively, studies such as Knupp et al. (2006) and Baker et al. (2009) point to differences in the thermodynamic profiles over land versus over water and suggest buoyancy is enhanced by surface heating over land.

While each of the above factors leading to environmental heterogeneity likely plays a role in individual cases, a study by Schenkel et al. (2021) combined TC tornado reports with VWS data derived from radiosondes to perform a climatology of TC tornadoes. Not to be confused with the total VWS available to any individual supercell, Schenkel et al. (2021) specifically characterized tornadoes as a function of synoptic-scale 850–200-hPa VWS regimes, which is representative of the background VWS acting upon the TC itself. The computation of the 850–200-hPa VWS involves removing the TC wind field to determine the background VWS. For clarity herein, we refer to the background, synoptic-scale 850–200-hPa VWS as the "background VWS" or "BVWS." The study showed that there were a disproportionate number of tornadoes within the first 50 km inland of the coastline [see Schenkel et al. (2021) and their Fig. 7] under all BVWS regimes. Although the TCs under strong BVWS spawned the most tornadoes at all coast-relative distances, the coast itself may influence TC supercells more strongly than the synoptic or even mesoscale environments in which the TC supercells are embedded.

Recently, Alford et al. (2020) used ground-based dual-Doppler analysis to characterize the hurricane boundary layer transition for a 12-h period during the landfall of Hurricane Irene (2011). Similar to the results of Hirth et al. (2012), an internal boundary layer response (i.e., the response of the boundary layer to an increase in surface roughness) was observed as parcels moved from over the ocean to over land. Using spatiotemporal average profiles from the dual-Doppler analyses, Alford et al. (2020) were able to show that the boundary layer wind field significantly changes within the first 10 km inland of the coastline, while little change is observed above the boundary layer. Such a drastic evolution of the low-level wind profile is likely to change the low-level shear available to TC supercells, in addition to coastal-scale convergence of the winds as discussed previously. Indeed, Novlan and Gray (1974), Gentry (1983), and Morin and Parker (2011) hypothesized that the low-level reduction and backing of the winds over land could lead to an enhancement of VWS. Additionally, Alford et al. (2023b) showed that tornadic mesocyclones were more intense onshore than their offshore counterparts using 8 years of radar-observed TC supercells, suggesting that processes at the coastal interface help to intensify tornadic mesocyclones.

Apart from the above case studies, a detailed analysis of the near-coast mesoscale environment has not been performed. Moreover, the coast's influence as a frictional boundary of sorts has yet to be documented in detail. This study employs a similar framework to that of Alford et al. (2020) to characterize the near-coast wind profiles in the outer bands of three TCs. Specifically, we seek to understand the role of near-coastal convergence and near-coastal changes to VWS that may enhance supercell mesocyclones. We emphasize that this study focuses specifically on supercells, not tornadoes. We document the structure of the VWS utilizing high-resolution dual-Doppler analyses to investigate whether the hurricane boundary layer transition can affect the mesoscale and storm-scale environments through which TC supercells are propagating. We also present the trends of TC supercell mesocyclone rotation as observed by ground-based radar, focusing on the low-level mesocyclone rotation intensity from ocean to land.

2. Cases and data analysis

a. SMART radar deployments

In this study, we leverage data collected by the Shared Mobile Atmospheric Research and Teaching (SMART) radars (SRs; Biggerstaff et al. 2005, 2021) to examine the kinematic mesoscale environment. The SRs are a pair (called SR1 and SR2) of C-band dual-polarization mobile weather radars built for observing convective and mesoscale phenomena. The SRs have observed numerous landfalling TCs since 2001. Three cases observed, Hurricane Frances (2004), Hurricane Irene (2011), and Hurricane Laura (2020), are particularly favorable for examining the outer bands. The SRs have been leveraged extensively in TC-based studies to examine convective and mesoscale processes (e.g., Hirth et al. 2012; Alford et al. 2019a,b, 2020, 2023a).

In both Irene and Laura, an SR (SR2 in Irene and SR1 in Laura) was paired with a nearby WSR-88D in order to

retrieve three-dimensional wind fields via dual-Doppler analysis (discussed in the following subsection). In Irene, the WSR-88D in Morehead City, North Carolina (KMHX), was used, and in Laura, the WSR-88D in Lake Charles, Louisiana (KLCH), was used. In Hurricane Frances, both SRs were employed as in Hirth et al. (2012). We note that Hurricanes Irene, Frances, and Laura were categorized at their official landfalls as category 1, 2, and 4 hurricanes, respectively. Here, we focus on the outer band environments, rather than the inner-core and eyewall regions. In Figs. 1a, 1c, and 1e, the tracks of the center of all three TCs can be seen relative to the dual-Doppler domain. In Figs. 1b, 1d, and 1f, plan position indicators (PPIs) of reflectivity from KMLB (Melbourne, Florida), KMHX, and KLCH, respectively, can be seen. The PPIs were collected in the outer bands, many of which contained supercell structures similar to those seen in the figure. In Frances, the observations were collected in the boundary layer of the right-front quadrant relative to TC motion and with the dual-Doppler domain origin more than 145 km from the TC center. In Irene, the observations were collected near the boundary of the right- and left-front quadrants relative to TC motion and with the dual-Doppler domain origin more than 190 km from the TC center. In Laura, the observations were collected in the right-front quadrant and with the dual-Doppler domain origin more than 115 km from the TC center.

b. *Wind syntheses*

Dual- and multi-Doppler wind synthesis is a commonly utilized method to combine radar Doppler velocity measurements to retrieve estimates of the full, three-dimensional wind often used in supercell and mesoscale convective system studies (e.g., Biggerstaff and Houze 1991; Yuter and Houze 1995; Wurman et al. 2007; DiGangi et al. 2016; Betten et al. 2018; Miller et al. 2020). In TCs, ground-based dual-Doppler analysis has also been successfully applied to boundary layer (e.g., Hirth et al. 2012; Kosiba and Wurman 2014; Alford et al. 2020) and convective-scale and mesoscale processes (e.g., Wingo and Knupp 2016; Fernández-Cabán et al. 2019; Alford et al. 2019a,b, 2023a). We use similar approaches in our analysis of all three cases. In Frances, we employ data from the SRs likewise used in Hirth et al. (2012). In Irene, the dataset from Alford et al. (2020) is leveraged. Described in more detail in Alford et al. (2020), dual-Doppler volumes in Frances and Irene were constructed by first quality controlling the data leveraging a variety of subjective (Oye et al. 1995) and objective (Helmus and Collis 2016; Alford et al. 2022) techniques. Then, the data were interpolated to a Cartesian grid following the method of Biggerstaff et al. (2021), which leverages natural neighbor interpolation (Sibson 1981). In Irene, spatiotemporally variable advection correction (Shapiro et al. 2010) was applied, as SR2 was not synced in time with KMHX. Finally, the wind syntheses were retrieved via a three-dimensional variational data assimilation dual-Doppler technique (Potvin et al. 2012). The method is nearly identical to the methods of Alford et al. (2023a). The dual-Doppler domains (described in Table 1) can be seen in Figs. 1a and 1c. In Frances, the Cartesian domain covers a similar region to that used in Hirth et al. (2012) and favors the easternmost domain, which was less affected by beam blockage. In Irene, the Cartesian domain covers only the northern dual-Doppler lobe as the southern lobe was severely contaminated by beam blockage (Alford et al. 2020).

As with any dual-Doppler study, error increases on the outer edges of a dual-Doppler lobe and can be exacerbated in larger domains (Doviak et al. 1976). In Frances and Irene, the small distance between the contributing radars yields better resolution and low-level coverage (Fig. 1). In this study, we also incorporate observations from Laura, which had a much larger domain and yielded much less sampling of the boundary layer. Therefore, we leverage a retrieval technique to estimate the horizontal wind using the Spline Analysis at Mesoscale Utilizing Radar and Aircraft Instrumentation (SAMURAI) technique. SAMURAI was developed in Bell and Lee (2012) for the purposes of leveraging a variety of observations to retrieve a maximum-likelihood estimate of the atmosphere. As in the Potvin et al. (2012) method, SAMURAI does not require integration of the mass continuity equation. In addition, both methods [i.e., the SAMURAI and Potvin et al.'s (2012) methods] can take in a background estimate of the atmosphere. SAMURAI goes further by minimizing the impact of boundary conditions and reducing the impact of interpolation assumptions on mass conservation through its spline-based approach [see del Moral et al. (2020) for further discussion]. By introducing a background estimate of the atmosphere and relying less on gridpoint interpolation, SAMURAI can help to minimize error inherent to dual-Doppler synthesis. Thus, the regions on the edges of the dual-Doppler lobe where the lower portion of the lowest radar elevation angle is used to estimate the lowest analysis level are more accurately computed, but we acknowledge there is larger error at the lowest analysis level due to undersampling.

The following steps were employed to retrieve the wind fields using SAMURAI in Hurricane Laura:

1) To create a background wind field, we employ mobile radiosonde launches that were conducted by the National Severe Storms Laboratory (NSSL) to the southeast of SR1. The location of the sounding launches is shown in Fig. 1e. Launches were conducted at 2346 UTC 26 August 2020 and 0238 and 0432 UTC 27 August 2020. The soundings were interpolated to a regular height grid (from 105 m altitude to 11 000 m every 100 m) and a regular time grid (from 0000 to 0400 UTC 27 August 2020 UTC at every 1 min) using linear interpolation. The resulting background horizontal wind speed is shown in Fig. 2. We note that the density profile is also derived from the time-interpolated soundings, which is used in the mass continuity constraint of SAMURAI similar to del Moral et al. (2020).
2) The SAMURAI analysis is then performed with KLCH and SR1 data as input data, resulting in a quasi-dual-Doppler analysis across the domain (detailed in Fig. 1 and Table 1). We refer to the analysis as a "quasi-dual-Doppler" analysis, as SAMURAI does not inherently limit the analysis to a 30° dual-Doppler cross-beam angle, and

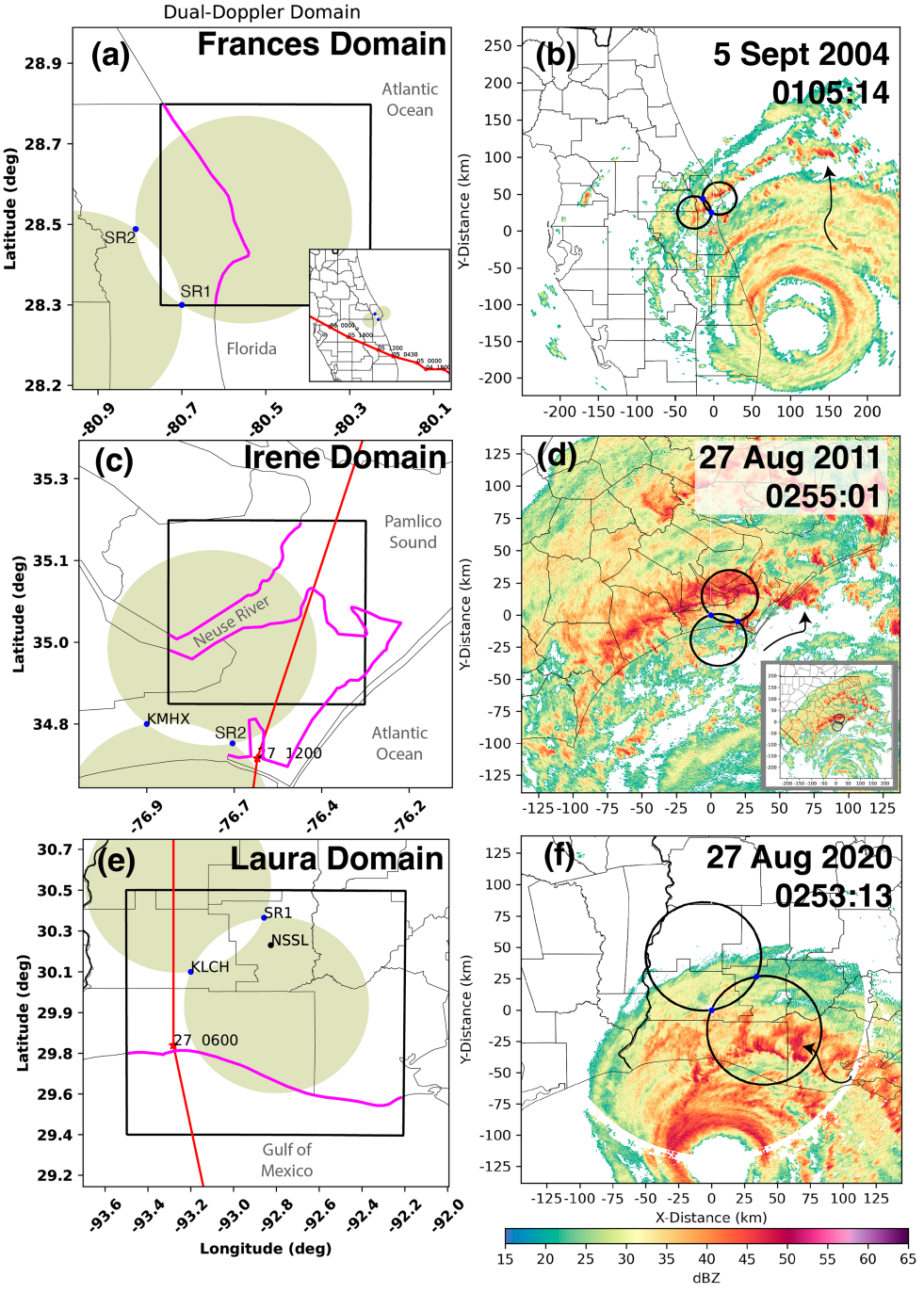

FIG. 1. Details of the dual-Doppler domains in (a),(b) Frances, (c),(d) Irene, and (e),(f) Laura are shown. In (a) and (c), the 30° dual-Doppler lobe is shaded, the locations of the radars are indicated by the blue dots, the heavy black box outlines the Cartesian dual-Doppler grid (although only the overlapping region between the dual-Doppler domain and the dual-Doppler lobes is utilized in the final analysis), and the red lines with the corresponding stars display the best track locations of each TC (with the day and hour/minute in UTC shown next to the star). For illustrative purposes, the areas of the coastline most pertinent to this analysis are shown in the bold magenta lines. In (a), the track is shown via the inset. In (e), the location of the NSSL radiosonde launches is shown via the black marker. In (b), (d), and (f), example PPIs of radar reflectivity (dBZ) are shown with the black lines showing the 30° dual-Doppler lobe for reference. The curved arrows point out examples of supercell-like structures in the PPIs. The date and times in the PPIs are in UTC. In (c), we also show an inset of radar reflectivity with a wider view for context to show the location of the center of Irene's circulation to the south of the dual-Doppler domain.

TABLE 1. Details of the radars contributing to the dual-Doppler analyses for each case including the radar names and their locations. Radar 1 is the radar at which the origin of the dual-Doppler domain is located. Radar 2 is the second radar in the dual-Doppler pair. The horizontal and vertical grid spacing is noted in kilometers. The terms x_{min}, y_{min}, and z_{min} denote the minimum locations of the Cartesian grid relative to the origin (Radar 1). The number of grid points along the x, y, and z directions x_{num}, y_{num}, and z_{num} is also documented. The baseline distance (distance between Radars 1 and 2) is also indicated.

	Frances (2004)	Irene (2011)	Laura (2020)
Contributing Radar 1	SR1	KMHX	KLCH
Contributing Radar 2	SR2	SR2	SR1
Radar 1 (lat, lon; °)	28.3415, −80.6876	34.7760, −76.8762	30.1253, −93.2160
Radar 2 (lat, lon; °)	28.5115, −80.7998	35.7331, −76.6620	30.3653, −92.8673
Horizontal, vertical resolution (km)	0.25, 0.1	0.25, 0.2	1.0, 0.5
x_{min}, y_{min}, z_{min} (km)	−20, −10, 0.2	5, 5, 0.2	−30, −80, 0.0
x_{num}, y_{num}, z_{num}	200, 200, 20	180, 180, 50	131, 121, 21
Times leveraged	1900 UTC 4 Sep 2004–0600 UTC 5 Sep 2004[a]	0000–0500 UTC 27 Aug 2011	0000–0315 UTC 27 Aug 2020
Baseline distance	21.8 km	19.0 km	43.2 km

[a] Note that the times leveraged are the same as in Hirth et al. (2012): 1900–1915, 1945–2000, 2145–2200 UTC 4 Sep 2004, 2345 UTC 4 Sep–0000 UTC 5 Sep 2004, 0300–0315, 0345–0400, 0500–0515, and 0545–0600 UTC 5 Sep 2004.

hence, the Cartesian grid is larger surrounding the 30° lobes in Fig. 1e. However, we do so upon output. The SAMURAI analyses are performed as in Bell and Lee (2012) and del Moral et al. (2020) where the Gaussian recursive filter length scale (in number of grid points) was set to 4 and 2 in the horizontal and vertical dimensions, respectively. The spline cutoff length was set to two grid points in all directions. We also allow adjustment of the background and impose a minimum of 10 dBZ echo for the wind field to be retrieved at any point.

3) We note that we allow a 0-m lowest analysis level in the SAMURAI system in order to prescribe the appropriate boundary conditions. However, it is not used and is replaced with an approximate 10-m wind vector (discussed next).

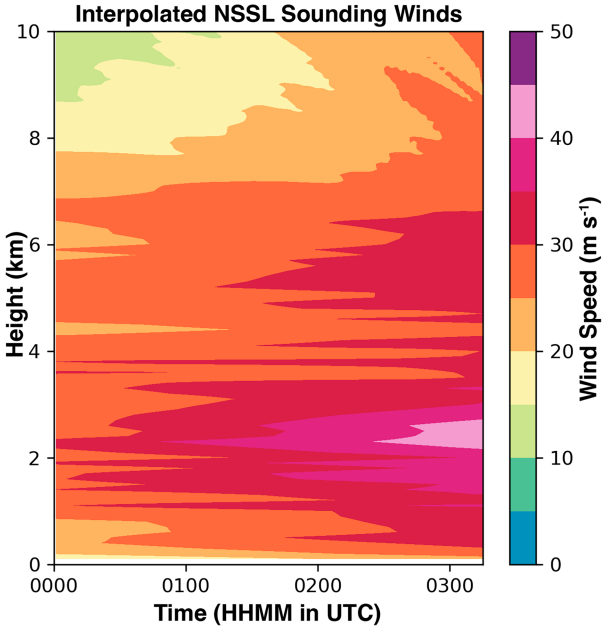

FIG. 2. Linearly interpolated horizontal wind speeds from NSSL sounding data.

We tested using SAMURAI in Irene, but ultimately elected to use the methodology of Alford et al. (2020) in Irene and Frances. Relatively dense (temporally) NSSL-launched soundings were available in Laura, where SAMURAI is a more beneficial technique to leverage. However, we found that the cubic-spline analysis technique, while advantageous in Laura due to the formerly described reasons, was detrimental to the Irene analyses above 7-km altitude. Gridpoint interpolation yielded a more continuous result following the method of Alford et al. (2020) in the increasingly data-sparse regions aloft between upper elevation angle radar PPIs. The problem is particularly exacerbated in Irene, as the smaller dual-Doppler domain on the whole is nearer the cone of silence of both radars. The same problem did not occur in Laura (due to the size of the dual-Doppler domain) or Frances (due to the shallow nature of the radar scanning strategies). However, it is also worth noting that in our tests of SAMURAI in Irene, we found that the resulting wind fields below 7-km altitude were nearly identical to the dual-Doppler results, suggesting limited sensitivity to our choice of method. Table 1 documents the domain details for the dual-Doppler analyses in Hurricanes Frances and Irene and the SAMURAI-based analyses in Laura. Since both analysis types retrieve the horizontal and vertical wind components as well as the reflectivity at each grid point, we simply refer to SAMURAI-based analyses as dual-Doppler analyses herein.

We also approximate the 10-m altitude winds from the lowest available dual-Doppler winds. We do so by leveraging the projection techniques discussed in Kosiba and Wurman (2014) and Alford et al. (2019b). In summary, 30-m land-use classifications obtained from the National Oceanic and Atmospheric Administration Coastal Change Analysis Program (available online at https://coast.noaa.gov/digitalcoast/tools/lca.html) are converted to an approximate surface roughness. Then, for each dual-Doppler point, the nearest 10 land-use surface roughness values are averaged. The lowest available

winds are then projected to 10-m altitude using a logarithmic profile assumption. In Irene and Laura, the 250- and 500-m altitude winds are used. In Frances, the very fine 100-m vertical resolution results in some missing data in the lowest few grid points mostly over the ocean. However, the same technique is used to project the lowest available wind to estimate the 10-m wind, since the projection is valid to use below the maximum wind altitude. Both Kosiba and Wurman (2014) and Alford et al. (2019b) showed good agreement between the projected estimates and in situ surface observations, but we do acknowledge some uncertainty with such a technique.

c. AzShear data and mesocyclone tracking

We also employ the use of single-Doppler azimuthal shear (commonly referred to as "AzShear"; Mahalik et al. 2019) to document the intensity of low-level mesocyclones without the constraints of the cross-beam limitations of dual-Doppler analysis. AzShear is a local, linear, least squares derivative of dealiased single-Doppler velocity data, which approximates to one-half of the total vertical vorticity. Hence, it can be used to quantify the intensity of low-level mesocyclones, particularly within 75 km of a weather radar.

In this study, besides using AzShear to estimate the intensity of individual mesocyclones, a tracking algorithm was employed to objectively identify supercells capable of producing a tornado (Sandmæl et al. 2023). We note that we did not discriminate between storms that did or did not produce a tornado, as storms need not be tornadic for the purposes of this work (i.e., we are interested in the mesocyclone response rather than tornado formation itself). This approach also eliminates uncertainties inherent to the TC tornado database (Edwards et al. 2012; Edwards and Mosier 2022). Storms with 0.5°-tilt single-radar AzShear above 0.006 s^{-1} were identified as supercells capable of producing a tornado and checked against a 20-dBZ reflectivity dilation filter to remove spurious noise not associated with an actual storm object. As discussed in Sandmæl et al. (2023), 0.006 s^{-1} represents a threshold that reasonably discriminates potentially tornadic versus nontornadic mesocyclones across all storms. The training and test datasets in Sandmæl et al. (2023) included TC supercell mesocyclones, which were tracked with similar success to Great Plains supercell mesocyclones and quasi-linear convective system mesovortices. In a recent study, Schenkel et al. (2023) confirmed that the 0.006 s^{-1} AzShear threshold reasonably discriminated between potentially tornadic and nontornadic mesocyclones in TCs. As in the Sandmæl et al. (2023) study, there was overlap between tornadic and nontornadic distributions near the 0.006 s^{-1} threshold and is not a perfect discriminator. Nevertheless, in our study each storm track was checked manually. Any storm not resembling a supercell at some point during its lifetime was removed. It is known that identifying a supercell in TCs can be difficult from weather radar (Spratt et al. 1997; Devanas et al. 2008; Martinaitis 2017; Nowotarski et al. 2021) largely due to their small sizes and less distinct radar characteristics when embedded within rainbands. In this study, the objectively tracked supercells (or supercell-like structures) were examined individually to confirm that 1) the AzShear maximum was associated with deep convection and 2) the radar attributes were reasonably characteristic of a supercell (e.g., high reflectivity and presence of a hook echo and/or forward-flank-like structure). We show examples of supercells retained in section 4.

d. BVWS computations

In Schenkel et al. (2020), BVWS was computed from the fifth major global reanalysis produced by European Centre for Medium-Range Weather Forecasts (ERA5; Hersbach et al. 2020). To calculate BVWS, Schenkel et al. (2021) removed the TC wind field for all 6-h International Best Track Archive for Climate Stewardship data, version 4 (Knapp et al. 2010), to characterize the BVWS for all TCs between 1980 and 2018 following prior work (Davis et al. 2008; Galarneau and Davis 2013). In summary, the synoptic winds are computed by first calculating the irrotational and nondivergent winds that characterize the TC. The irrotational and nondivergent winds are then removed from the TC total wind field to retrieve the background synoptic-scale horizontal wind field. However, rather than leveraging the BVWS magnitude and direction directly as in the Schenkel et al. (2021) study, we retain the background synoptic-scale horizontal wind field used to compute the BVWS and convert it to the local dual-Doppler height grid. Specifically, the wind field is available on the ERA5 output grid on isobaric levels with vertical grid spacing of 25–50 hPa. Thus, the 6-h synoptic winds are linearly interpolated onto the vertical dual-Doppler grids for direct comparison.

e. Coastal compositing

As in Alford et al. (2020), we employ a simple compositing technique using dual-Doppler observations to characterize the deep-layer VWS relative to the coast. Dual-Doppler radar observations collected in the outer bands of the TC cases are temporally and spatially averaged through the following steps:

1) For each x, y location on the dual-Doppler grid, we first calculate the distance (regardless of wind direction) to the nearest point on the coast, computed from the Global Self-Consistent, Hierarchical, High-Resolution Geography Database (Wessel and Smith 1996). While computing the coast-relative distance as a function of wind direction (i.e., the fetch an air parcel travels over land) may yield different results, we employ the compositing method of Alford et al. (2020) for consistency, because a more rigorous trajectory-based analysis would require three-dimensional wind retrieval regions much larger than the dual-Doppler domains in this study. When accounting for coast-relative distance, we removed the small coastal waterways in the Frances dataset and the inland lakes from the Hurricane Laura dataset. We retain the relatively large coastal waterways in the Irene dataset (e.g., the Neuse River and Pamlico Sound in Fig. 1a), as they serve as proxies for offshore water surfaces (discussed and validated in Alford et al. 2020).

2) VWS (also known as the bulk wind difference) is defined as the magnitude of the vector difference in the winds between two layers. Here, the VWS is computed by subtracting the u and v components of the wind at the 10-m height from each u and v wind observation at each height z. We compute VWS for each x, y location in the dual-Doppler domain for each analysis time t as in Eq. (1):

$$\mathrm{VWS}(x,y,t) = \sqrt{[u(x,y,z,t) - u(x,y,z = 10,t)]^2 + [v(x,y,z,t) - v(x,y,z = 10,t)]^2}. \quad (1)$$

3) As discussed in Franklin et al. (2003), Zhang et al. (2011), and Alford et al. (2020), comparing wind profiles in varying flow regimes (i.e., changes in the vertical structure and/or magnitude of the flow) requires normalization of the wind profiles. Therefore, we also compute the normalized wind magnitude at each x, y location by dividing the wind magnitude at each height in a column by the mean wind at and below 500 m in the column following Alford et al. (2020). We then retrieve the normalized u and v components of the wind. To compute the normalized VWS, we then subtract the 10-m normalized u and v components from each z-km observation to generate the normalized u and v components of VWS. The normalized VWS is then the magnitude of the former vector and shown in Eq. (2):

$$\mathrm{VWS}_{\mathrm{Norm}}(x,y,t) = \sqrt{\left[\frac{u(x,y,z,t) - u(x,y,z = 10,t)}{u(x,y,z = 10:500,t)}\right]^2 + \left[\frac{v(x,y,z,t) - v(x,y,z = 10,t)}{v(x,y,z = 10:500,t)}\right]^2}. \quad (2)$$

4) Finally, in 2.5-km bins relative to the coast, the horizontal wind magnitude, the individual u and v components (both total and normalized) of the horizontal wind, the divergence, the VWS, and the normalized VWS are averaged over space and time. Here, we define positive and negative distances relative to the coast as over water and over land, respectively.

We note that we do not remove supercells themselves from the coastal compositing. The supercells here typically are $O(10)$ km in their longest dimension and are often short lived (Spratt et al. 1997; Martinaitis 2017). When considering the dual-Doppler area and when considering that the composites are built over hours of dual-Doppler analysis, they constitute a small fraction of the dual-Doppler observations. We tested the sensitivity of the results by removing profiles in Laura with absolute vertical velocities that exceeded 5 m s^{-1} (analysis not shown). We found negligible differences in the composite results. Nevertheless, we not only acknowledge some "contamination" of the supercells on the composites but also emphasize that it is difficult to separate the effects of supercells on their environment (Parker 2014; Nowotarski and Markowski 2016; Wade et al. 2018).

3. Coastal transition deep-layer VWS

a. *Coastal-composite kinematics*

We first examine the coastal-composite kinematics in Hurricanes Frances and Irene. Both of these cases have been previously examined in terms of how the boundary layer winds respond to the increase in surface roughness at the coast (Hirth et al. 2012; Alford et al. 2020). In both cases, an internal boundary layer response (Garratt 1990) was observed wherein the flow within the forming internal boundary layer decelerated and the flow above the boundary layer remained quasi steady. Again, the observations were taken near the boundary of the left-front (partly in Irene) and right-front (both Frances and Irene) quadrants relative to TC motion in the outer bands. As noted in Hirth et al. (2012) and Alford et al. (2020), the flow in both cases has a significant eastward component (mean 0–2-km and 0–3-km wind directions of 70° and 98° in Frances and Irene, respectively, meaning the flow is onshore from the Atlantic Ocean toward Florida and North Carolina in Frances and Irene, respectively), although we further discuss some of the local coastline effects on the analysis.

As noted in both Hirth et al. (2012) and Alford et al. (2020), periods when a parcel traversed land and moved back over water are important to consider when examining the near-coastal internal boundary layer response. In Alford et al. (2020), specifically, the flow in Irene observed over water was found to be representative of open-ocean dropsonde profiles taken well offshore, although at times parcels had likely previously interacted with land surfaces. Both studies of Frances and Irene focused on the lowest few kilometers of the atmosphere. Here, we begin with a similar analysis in Frances, but extend the analysis of the coastal-composite wind field through the full depth of the dual-Doppler volumes in Irene, which leveraged much deeper radar volumes than were used to observe Frances. We first examine the coast-relative composite kinematic environment in Fig. 3, but with the addition of the estimated 10-m winds as described in section 2. Consistent with both Hirth et al. (2012) and Alford et al. (2020), the coast-relative composite wind profiles (Figs. 3a,d) show that the wind profile below 1 km changes inland. In particular, the

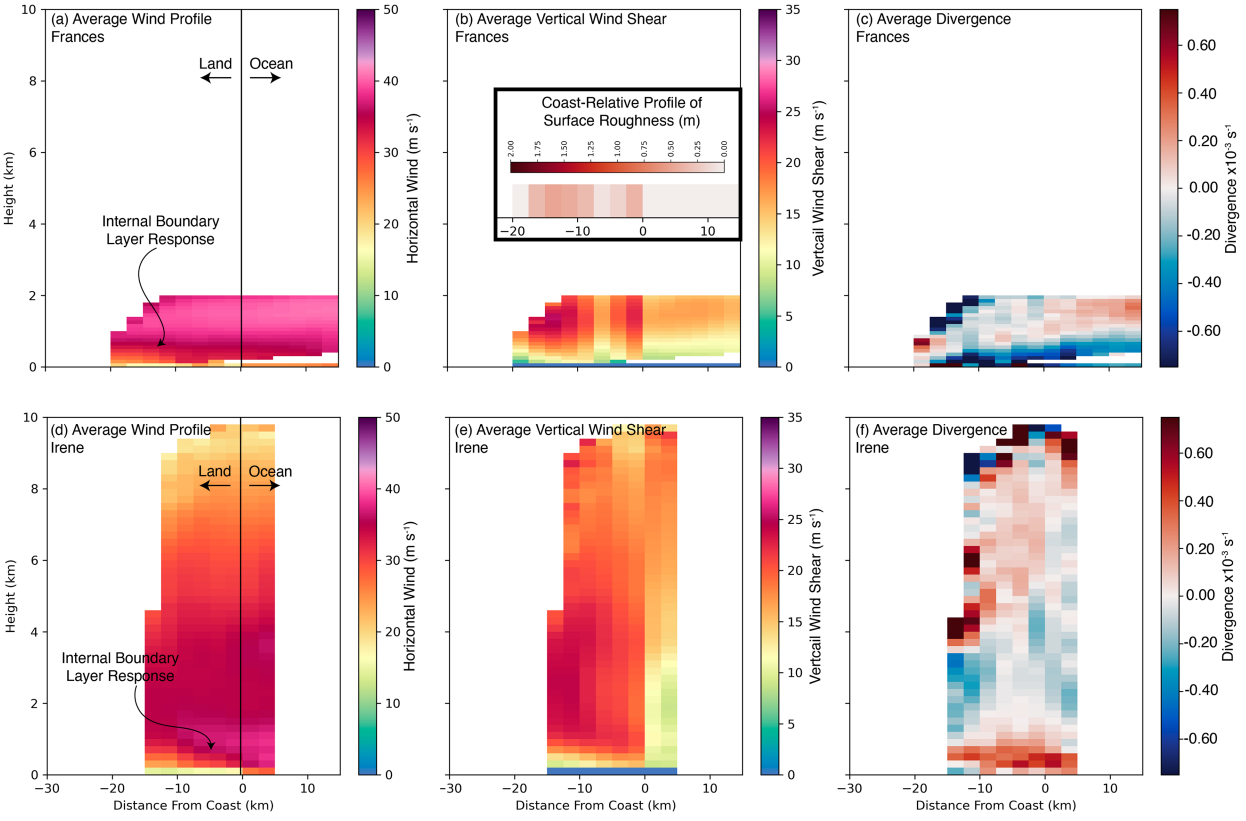

FIG. 3. The dual-Doppler coast-relative composite (a) horizontal wind speed, (b) VWS (i.e., the total VWS), and (c) horizontal divergence in Hurricane Frances are shown as a function of coast-relative distance on the *x* axis and height on the *y* axis. (d),(e),(f) As in (a), (b), and (c), but for Irene. For reference, a value of 0 km on the *x* axis is the coast and negative distance is over land and is annotated in (a) and (c) by the vertical black line. The inset in (b) shows the coast-relative area-mean surface roughness.

low-level winds reduce over land compared to those over the ocean. The low-level wind speed reduction grows in height deeper inland. However, above 1–2-km altitude the horizontal winds change more slowly as a function of coast-relative distance. The corresponding VWS (Figs. 3b,e) increases over land. For example, over the 0–1-km layer, the VWS over the ocean in both cases is near 15 m s^{-1} compared to values of 20–25 m s^{-1} over land. In Irene, specifically, over a deeper layer (e.g., the 0–6-km layer), a similar response is seen with VWS increasing over land compared to the shear over water. We also note that in very shallow layers (e.g., 0–0.25-km layers), which are likely pivotal for tornadogenesis (Coffer et al. 2019), there are actually decreases in VWS inland relative to the deeper-layer VWS (i.e., the 0–1, 0–3, or 0–6-km VWS) previously discussed. The maximum in very low-level VWS in both analyses tends to be very near the coast.

There are notable minima in VWS in the Frances case (Fig. 3b) from −5 to −7.5 km inland and from −17.5 to −20 km inland. Noted in Hirth et al. (2012), two inland waterways are located within the dual-Doppler domain. While Hirth et al. (2012) did not composite their dual-Doppler data as we do here, we can determine the effects of the inland waterways on the mean wind and VWS profiles by similarly compositing the surface roughness estimates as described in section 2e. As shown in the inset of Fig. 3b, area-averaged surface roughness decreases from −5 to −17.5 km inland, corresponding with minima in the VWS profiles. This result is consistent with the work of Hirth et al. (2012), who documented that the internal boundary layer response is a function of the underlying complexity in land-use characteristics. We find similar results here in terms of VWS. Although the surrounding coastal region in Irene is quite complex (i.e., there are many inland waterways, peninsulas, and islands), the coastal region specifically within the dual-Doppler domain (Fig. 3e) is characterized by only one ocean surface (the Neuse River and Pamlico Sound) and one land surface (the land surrounding the waterways). Although the flow did at times first cross other land surfaces prior to entering the Neuse River and Pamlico Sound, the dual-Doppler domain in Irene was too small to further examine the more complex internal boundary layer response. Nevertheless, internal boundary layer response in the low-level wind speed appears to lead to an increase in VWS over land surfaces in the Irene case, consistent with the results in Frances.

As noted previously, near-coastal convergence of the low-level horizontal wind has been hypothesized to enhance the vertical drafts of individual storms (e.g., Baker et al. 2009). In the same coast-relative framework, we show the coastal-

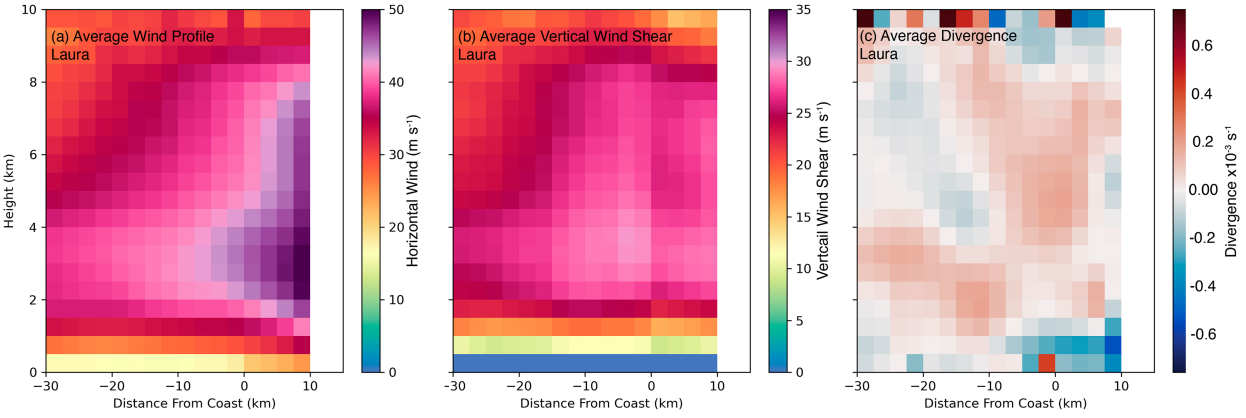

FIG. 4. As in Fig. 3, but for Hurricane Laura.

composite profile of horizontal divergence in Figs. 3c and 3f. In Frances, we find that significant convergence (negative divergence) is observed in the low levels of the analysis in the onshore flow. In contrast, positive divergence is observed in the lowest 1 km in a coast-composite sense both onshore and offshore in Irene. We further examined why convergence was not seen in the generally onshore flow (flow from the east) throughout the period. It was found that flow from the east first crossed from Pamlico Sound onshore and then offshore again over the Neuse River (see Fig. 1). Divergence was particularly maximized spatially when composited in time over the regions surrounding the Neuse River (not shown). Therefore, the divergence in the low levels likely is a result of the complex coastal structure in Irene, suggesting that the presence of divergent or convergent flow is not necessarily ubiquitous in the near-coastal zone, but rather is a function of the upwind surface characteristics.

b. *Estimating VWS in Hurricane Laura*

As discussed in section 2b, the use of SAMURAI in retrieving the wind field in Hurricane Laura helps to minimize (but not eliminate) the errors associated with undersampling the lowest analysis level, particularly since the aim of this study is to determine the effects of the boundary layer transition (a low-level feature) on VWS. Hurricane Laura was characterized by onshore flow (any wind with a northerly component was removed from the analysis), but a significantly lesser component thereof (100° mean wind direction during the times analyzed, meaning flow was mostly from the east with a small component from the Gulf of Mexico toward Louisiana). Nevertheless, we still examine the coastal-composite wind profiles in Laura as in the previous analyses. A similar coastal-composite analysis is shown for Hurricane Laura in Fig. 4. The wind magnitude in Fig. 4a is stronger than in Hurricane Frances or Irene with Laura being a category 4 (58–70 m s^{-1}) hurricane near landfall (Pasch et al. 2020). Laura was also a smaller, more compact TC than Irene, meaning that the outer bands were located nearer the center of the circulation (Fig. 1). We note that the gradient in the average wind profile is partly due to stronger winds near the inner core first arriving in the offshore bins (and explore such effects further in section 3d). Similar to the evolution in Irene, the low-level wind speed in Laura (Fig. 4a) decreases over land. A gradient in the low-altitude winds (below 2 km) in Fig. 4a is seen, similar to the results of both Frances and Irene. Although the near-coastal regions are undersampled by the radars contributing to the analysis, the SAMURAI-based analysis reveals a signal of decreasing winds in the low levels, but over a deeper layer than seen in Frances or Irene. Between −10 and 0 km, the mid- and upper-level wind speed (above 4–5 km) varies relatively little as a function of coast-relative distance, but weakens between −30 and −10 km. It is likely that the effects of the coast-relative compositing versus the prevailing wind direction explain some differences between the Frances and Irene analyses versus the Laura analyses. The onshore component in Laura is not well aligned with the gradient in coast-relative distance as approximated by the nearest point on the coast (generally a north–south gradient in Laura). As such, the composite results here are more strongly representative of the cross-internal boundary layer response, rather than the along-internal boundary layer response.

With the differences between the Frances and Irene analyses versus the present analysis in mind, Fig. 4b shows the coastal-composite VWS. There are two maxima in VWS: one just inland between −15 and 0 km inland and one over water. In particular, 0–3-km VWS increases from 25 to 30 m s^{-1} over water to >30 m s^{-1} over land. Taking similar layers (e.g., the 0–6 or 0–1-km layers) yields similar increases in VWS inland versus over water. Deeper inland in the coast-relative composite, there is a general decrease in VWS, likely where parcels have longer histories over land. In Laura, we find that the VWS increase is maximized between −10 and 0 km. We also examine the coastal-composite divergence (Fig. 4c). Like in Frances, the coastal-composite mean divergence field is generally convergent in the low levels (<1-km altitude) of the near-coastal (>−10 km) region. In this zone, convergence is maximized in the low levels between 0 and −5 km offshore unlike the preceding analysis of Irene, but like the preceding analysis of Frances. This is likely due to a less complex coastline compared to that in Irene, suggesting that the onshore

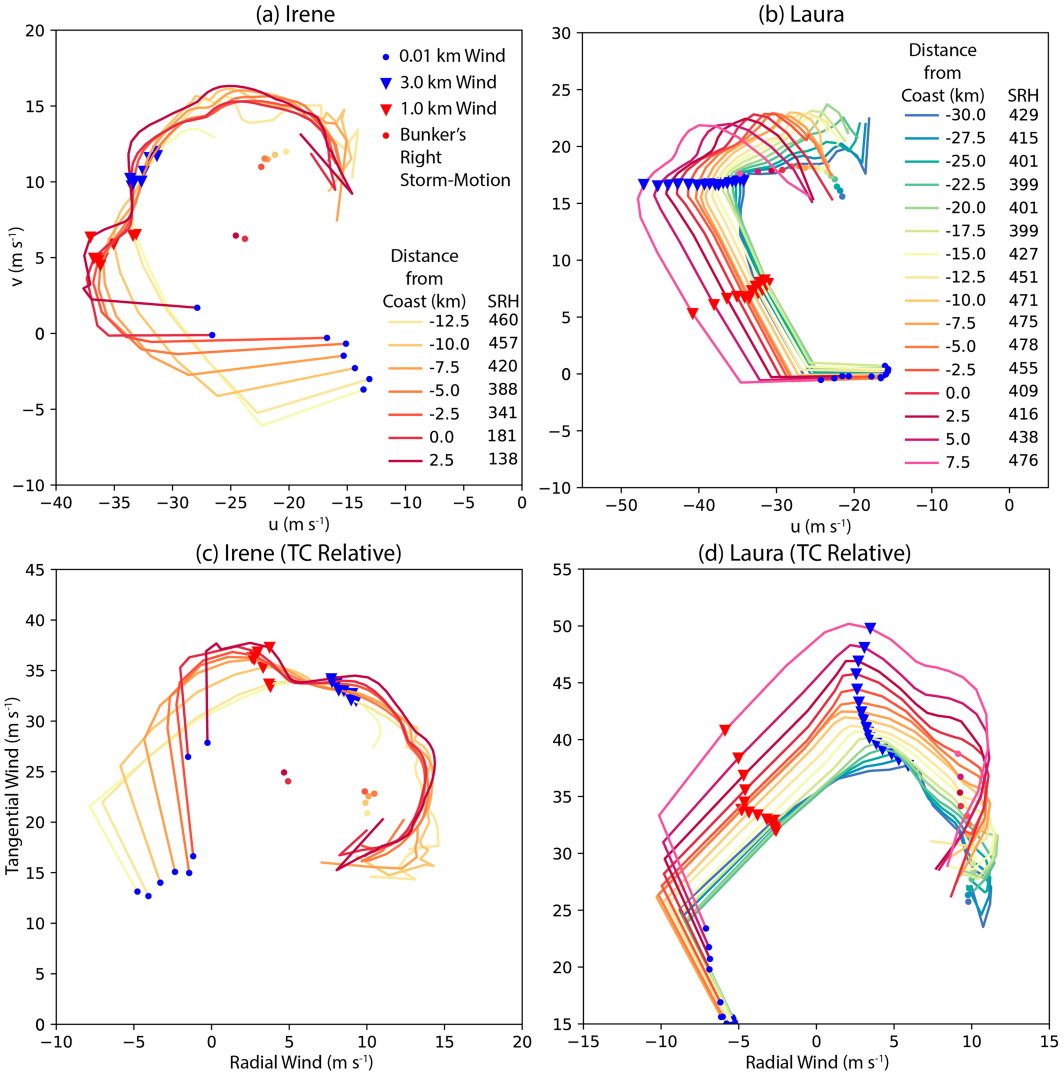

FIG. 5. Composite hodographs based on the wind profiles shown in Figs. 3 and 4 for (a) Irene and (b) Laura. The blue dots indicate the wind at the estimated 10-m wind. The red triangle denotes the 1.0-km wind. The blue triangle denotes the 3.0-km wind in each hodograph. The lines (dots) indicate the hodographs (Bunkers right storm motion) at each coastal bin according to the legend. The 0–3-km SRH ($m^2 s^{-2}$) is also shown in the legend. (c),(d) The same hodographs as (a) and (b), but as a function of the tangential and radial winds relative to the TC center location. The TC centers were found as in Alford et al. (2020).

flow response does indeed result in a zone of convergence in the coastal zone both over land and over water, similar to the results of Frances and to past studies discussed in section 1.

c. *Storm-relative helicity*

We also examine the evolution of the outer band environments as a function of coast-relative distance using storm-relative helicity (SRH; Davies-Jones 1984) and hodographs. Using the coast-relative binned wind profiles of u and v described in section 2e, composite hodographs in only Hurricanes Irene and Laura are shown in Figs. 5a and 5b, respectively. We employ the SRH computation in Ramsay and Doswell (2005), where SRH is computed from the Bunkers right storm motion (Bunkers et al. 2000) using a 0–8-km (rather than 0–6 km as in the original Bunkers method) density-weighted mean wind that is adjusted using a 7.5 m s^{-1} right deviation. The corresponding supercell storm motion in this case was computed through the coastal-compositing method as in the prior sections, but limited to dual-Doppler points where continuous observations were available between the lowest dual-Doppler level and 8-km altitude. Since the analyses in Frances are limited to altitudes below 2 km, Frances is not examined in this portion of the analysis. The mean wind profile was weighted by the time-interpolated sounding density profile described in section 2b (in Irene, we time interpolated

the 0000 and 0600 UTC 27 August 2011 soundings from the National Weather Service to retrieve density). The Bunkers right motion for each coast-relative hodograph can be seen in Fig. 5. For simplicity, herein we refer to the 0–3-km SRH simply as "SRH." We note that the SRH computations are sensitive to the validity of the 10-m wind projection method. Therefore, we likewise computed the SRH between the lowest dual-Doppler analysis level and 3 km and found the results herein were qualitatively similar (i.e., the trends in SRH as a function of coast-relative distance were the same) but quantitatively different (i.e., the SRH computed using the 10-m wind was larger as expected).

In Irene, the hodographs (Fig. 5a) primarily change below 3-km altitude. In particular, the winds below 0.5-km altitude decrease in magnitude. In TC relative space (Fig. 5c), the tangential wind slows inland, and the radial wind component becomes more negative (stronger inflow toward the center of the TC). Above 3 km, however, there is little change in the winds across all hodographs, again suggesting that the low-level wind field adjustment is primarily responsible for changes in the kinematic environment. As such, the SRH values at each coastal bin increase over a 15-km distance. Just over water at +2.5 km, the SRH is 138 $m^2 s^{-2}$ but increases to 460 $m^2 s^{-2}$ at −12.5 km (Fig. 5a).

In Laura (Fig. 5b), larger changes above 3-km altitude can be seen in the hodographs compared to Irene. Nevertheless, compared to the winds below 3 km, the winds aloft changed slower than those below 3 km. A substantial decrease in primarily the u component of the winds below 3 km is noted in Laura. The v component of the wind changes little. As discussed previously, the results in Laura are more representative of the cross-internal boundary layer response, which is consistent with the results of the hodographs. Nevertheless, a change in SRH as a function of coast-relative distance is observed. Two maxima in SRH are noted at −5 km inland and +7.5 km offshore. The latter maximum offshore, also seen in the coastal-composite VWS (Fig. 4b), is likely attributable to the changes in the mean wind profiles as a function of radius in the TC. The topic is addressed in the next subsection. We also note the decrease in SRH deeper inland. Like in the VWS analysis (Fig. 5), the decrease in SRH is likely due to the coast-relative profiles deeper inland being representative of parcels with longer histories over land. As such, the effects of the internal boundary layer response on VWS and SRH appear largely confined to the near-coastal zone prior to the more complete adjustment of the winds through a deeper layer.

d. *Normalizing the wind profiles*

While changes in the VWS and SRH discussed previously indicate that VWS and SRH are maximized inland, the results in Laura in particular indicate an offshore maximum in VWS and SRH. We hypothesize that this is due to the outer regions of the inner core entering the outer edge of the dual-Doppler domain as Laura moved northward (i.e., the mean wind increased in the offshore bins first). Thus, we explore VWS and SRH in terms of normalized wind profiles, rather than in terms of their raw values as in Figs. 3–5. We do so to compare wind profiles of varying vertical structure or mean magnitude as described in Zhang et al. (2011) and Alford et al. (2020) in order to better isolate the effects on the wind profile from the coast itself.

Figures 6a and 6b show the normalized VWS for Irene and Laura according to Eq. (2). When composited in coast-relative space, the highest values of normalized VWS are indeed inland and maximized near −10 km in both cases for all layers. The normalized VWS structure in Irene (Fig. 6a) largely mirrors the total VWS seen in Fig. 3b. This finding is not surprising given that the structure and magnitude of the wind profiles in the outer bands varied little through space and time (Alford et al. 2020). In category 4 Laura, the radial gradient of the horizontal wind at all heights was significantly stronger than in Irene, yielding a gradient in the wind profiles across the dual-Doppler domain. The normalized VWS in Laura is strongest inland. However, we note that it is possible that normalized VWS can increase without an increase in the total VWS, since the normalized VWS is relative to the low-level wind. In Irene, the total VWS tends to increase and the low-level winds tend to decrease over land, suggesting the increase in normalized VWS is consistent with the results of the total VWS evolution relative to the coast. In other words, the change in total VWS is related to the onshore flow and subsequent boundary layer transition. In Laura, the normalization of the VWS profile yields the ability to interpret the changes in VWS regardless of the background wind regime changes. In Fig. 4b, the maximum in total VWS is over land (with a corresponding relative minimum in the low-level wind), suggesting that the maximum in normalized VWS is at least in part attributable to an over land maximum in total VWS. However, the relatively small increase in total VWS/SRH between land and ocean suggests that the contrast between land and ocean in Laura is more muted than in Irene (or Frances). We discuss this result in the context of the flow direction relative to the coastal geometry in section 5.

We also examine the evolution of the coastal-composite hodographs in normalized wind space in Figs. 6c and 6d. The normalization of the u and v wind components was described in section 2e. Similar to the SRH computations in section 3b, we likewise compute a "normalized SRH" over the 0–3-km layer using a density-weighted Bunkers right supercell storm motion. However, one modification in the Bunkers right motion had to be employed. The Bunkers right deviation from the mean wind is typically 7.5 m s^{-1} (Bunkers et al. 2000). For each wind profile, we computed the normalized deviation D at each dual-Doppler grid point for all dual-Doppler times by dividing D by the mean wind at or below 500-m altitude to yield D as a function of x, y, and t. Then D was composited as in section 2e to prescribe the proper adjustment to the mean wind in the SRH computation.

Similar to VWS, the normalized hodographs suggest that the most substantial changes in the normalized wind profile occur below 3-km altitude and are particularly prominent below 1-km altitude. The corresponding normalized SRH increases inland, similar to the full SRH in Fig. 5c. In Laura (Fig. 6d), the hodographs are elongated largely due to changes in the 3-km altitude winds. We note that the increase

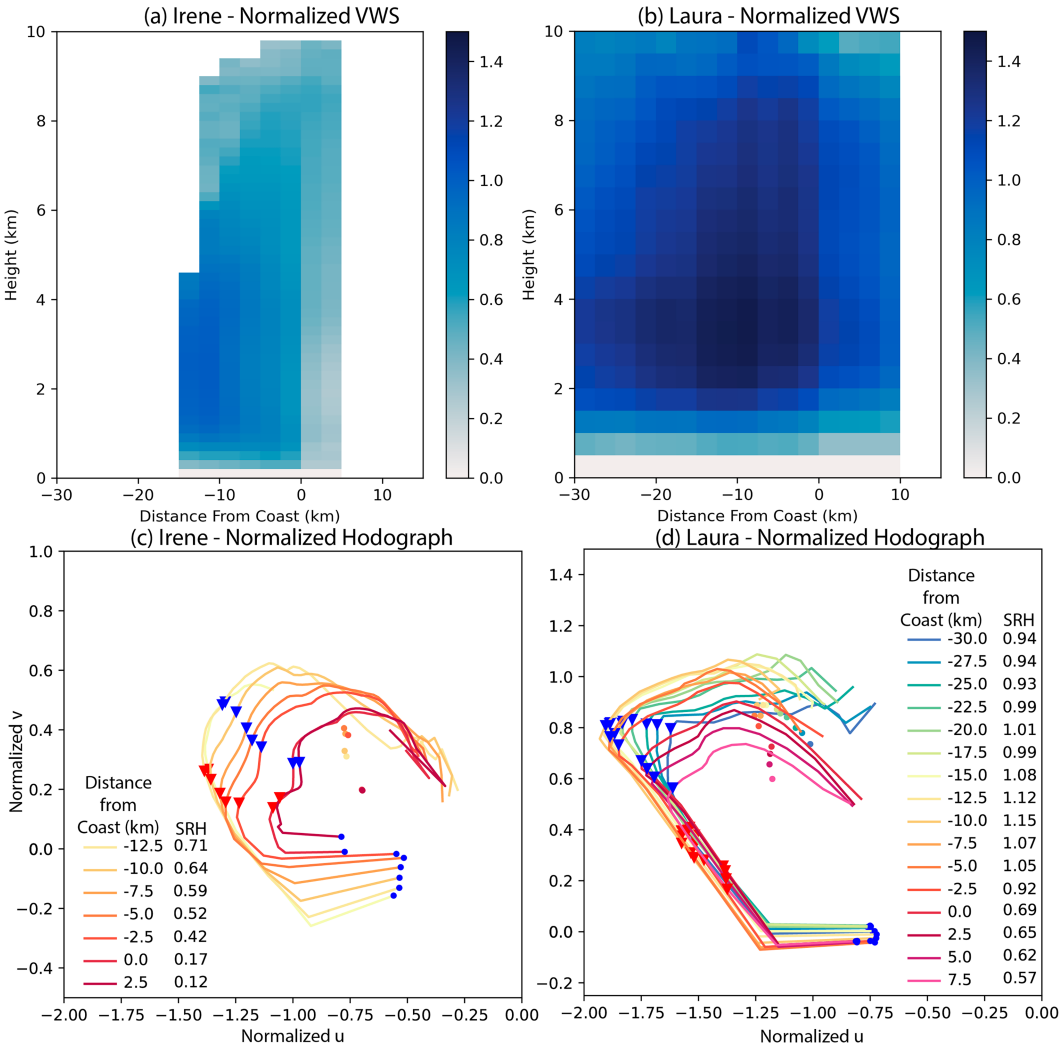

FIG. 6. As in Figs. 3b and 4b where VWS is shown for Irene and Laura, respectively. (a),(b) The coast-composite normalized VWS values according to Eq. (2). Similarly, the normalized hodographs for (c) Irene and (d) Laura are shown. As in Fig. 5, the SRH is shown in the legend (unitless), the 10-m wind is shown by the blue dots, the 1-km wind is shown by the red triangles, and the 3-km wind is shown by the blue triangles.

in the 3-km winds does not reflect an increase in the actual wind, but rather an increase in the wind near 3-km altitude relative to the changes in the low-level wind (i.e., the low-level winds are decreasing). However, it is clear that these changes manifest in an increase in normalized SRH, which is maximized at −10 km inland. The result is similar to the full composite hodograph in Fig. 5d and suggests that SRH increases inland for similar wind profiles. We note that for the same reasons as described in the discussion of normalized VWS, the normalized SRH values in Laura do suggest an increase in SRH over land, but with a more muted response between land and ocean. We also note that no offshore maximum exists in either the VWS or SRH space upon normalization, suggesting that the offshore maximum seen in Figs. 4b and 5b is the result of the advancing inner core, which was characterized by a stronger wind profile, and increasing total VWS and SRH. This result is consistent with the results of Bogner et al. (2000), Franklin et al. (2003), and Nowotarski et al. (2021), for example, who showed that VWS typically increases toward the center of circulation.

e. *Effects of BVWS*

We next turn to the effects of BVWS on the near-coastal environments in Irene and Laura (we again neglect Frances due to the shallow nature of the dual-Doppler volumes). As discussed in section 1, near-coast supercell tornadoes are not directly explained by the synoptic environment in which the TC is embedded (i.e., the BVWS; Schenkel et al. 2021). However, the total TC tornadoes (regardless of coast-relative distance) are related to the BVWS. Thus far, the VWS examined is related to the total horizontal wind field which includes the background synoptic wind field $\mathbf{u}_{\text{synop}}$. However, by removing

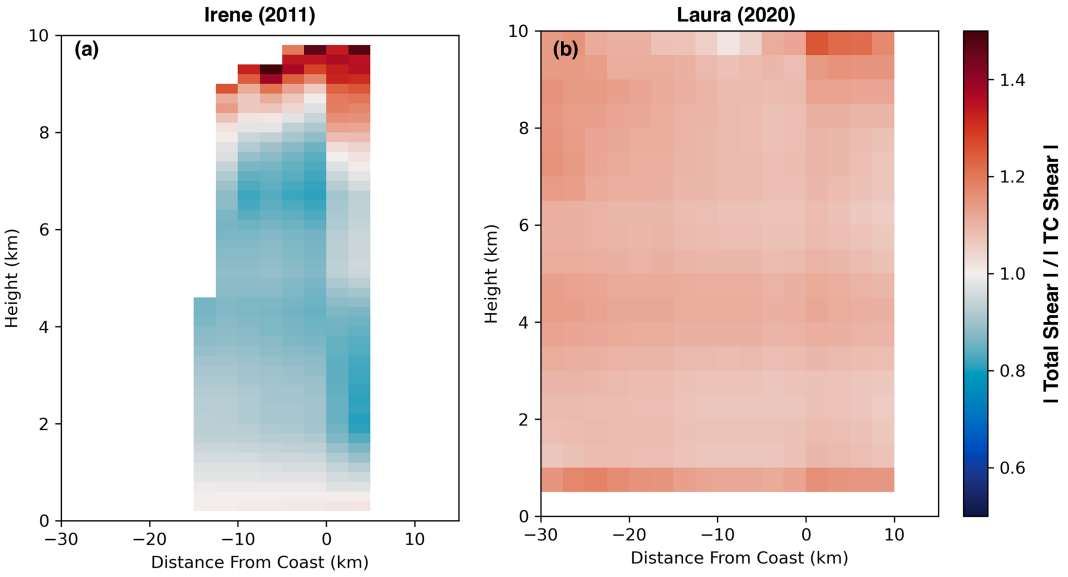

FIG. 7. The ratio of the VWS to the TC-only VWS is shown as a function of coast-relative distance (x axis) and height (y axis). Values > 1 indicate that the magnitude of the VWS (including the synoptic-scale wind field) is stronger than the TC-induced shear.

$\mathbf{u}_{\text{synop}}$, we compute the TC-induced wind field $\mathbf{u}_{\text{TC}}$. Thus, Eq. (3) shows the VWS as a function of $\mathbf{u}_{\text{synop}}$ and $\mathbf{u}_{\text{TC}}$, where z denotes the height and a subscript 0 denotes the 10-m estimated dual-Doppler level:

$$\mathbf{VWS} = \mathbf{u}_{\text{TC}}(z) + \mathbf{u}_{\text{synop}}(z) - (\mathbf{u}_{0\text{TC}} + \mathbf{u}_{0\text{synop}}). \quad (3)$$

Hence, VWS with the synoptic windfield removed VWS_{TC} is assumed to be the result of only TC itself and is shown in Eq. (4):

$$\mathbf{VWS}_{\text{TC}} = \mathbf{VWS} - [\mathbf{u}_{\text{synop}}(z) - \mathbf{u}_{0\text{synop}}]. \quad (4)$$

By taking the ratio of the magnitudes of the VWS to the VWS_{TC}, we ascertain the superposition of the synoptic wind on the near-coastal VWS structure. We note that we assume the synoptic winds to be constant across the TC and do not account for the (assumed) small change in the synoptic wind that would occur over land. For reference, the BVWS is constructive when $\text{VWS}/\text{VWS}_{\text{TC}} > 1$. Figure 7 shows the ratio of the VWS to the VWS_{TC}. In both Irene (Fig. 7a) and Laura (Fig. 7b), the layers where $\text{VWS}/\text{VWS}_{\text{TC}} > 1$ are generally those that include mid- and upper levels. More specifically, in Irene the BVWS is constructively superimposed at altitudes above 8 km, whereas in Laura the BVWS is constructively superimposed at all heights. In both cases, the ratio becomes larger over a deeper layer, suggesting that the BVWS may be more constructive to the total VWS profile. In Laura, the greatest superposition appears to be in the lowest analysis level. In the low levels of Irene (e.g., 0–3 km), the ratio is generally less than 1 implying that the VWS associated with the TC itself is most impactful to the total VWS profile, consistent with Schenkel et al. (2020). In the case of Laura, the 0–3-km layer is slightly >1, implying that the BVWS contributes constructively to the total VWS. It is difficult to draw conclusions on the general relationship between the number of tornadoes and the effects of BVWS on them directly (e.g., the superposition of BVWS on the low-level VWS), particularly since Irene had more confirmed tornadoes near the coast than confirmed in Laura according to the Storm Prediction Center TC tornado (TCTOR) data (Edwards and Mosier 2022). However, two conclusions may be drawn:

1) The deep-layer VWS is enhanced by BVWS in these two cases and is likely integral to convective organization as found in previous studies (e.g., Schenkel et al. 2020, 2021).
2) Regardless of the low-level effects of BVWS on the total VWS, the effects of the boundary layer transition on total VWS yield greater VWS and SRH immediately inland in both cases examined, particularly when the effects of radial gradients of wind speed are removed.

4. Response of individual supercells

The former section characterized the coast-relative composite VWS and SRH environments through which an individual supercell storm may move. It is yet unclear how the environmental changes project onto storm-scale structure, particularly the low-level mesocyclone intensity. Alford et al. (2023b) explored such changes for 8 years of TC supercell data and showed evidence that tornadic supercells tend to intensify as they cross the coastal boundary. The results of the Alford et al. (2023b) study are consistent with the environmental analysis in section 3 such that TC supercell mesocyclones are expected to intensify as they move inland into a higher

VWS and SRH regime. Nevertheless, we explore this hypothesis further here using single-Doppler radar in Irene, which was optimal for tracking strong mesocyclones as they moved onshore. We do not explore the same in Laura, since the observations from KLCH were not optimal to track mesocyclones >10 km offshore. We note that by leveraging single-Doppler data, our analysis is not limited to the dual-Doppler domains as in Fig. 1.

We first examine the individual storms tracked (in total nine) in Hurricane Irene to verify the tracking algorithm indeed tracked TC supercell storms. TC supercells are often characterized by a hook echo in radar reflectivity and are associated with a persistent low-level mesocyclone (Spratt et al. 1997). Thus, we examined each individual case to confirm that both criteria were met along the supercell track. Because of our strict criteria, we may eliminate some supercells that are not well resolved by weather radar (Devanas et al. 2008; Martinaitis 2017). We show a subset of examples in Fig. 8 of supercells with the distinguishing characteristics of 1) hook echoes in reflectivity on the eastern portions of the storms (since the supercell storm motion is to the west) and 2) prominent AzShear maxima near and to the north of the hook echo signatures.

We next examine the intensity of nine individual supercell mesocyclones in the outer bands of Irene (Fig. 9a). The tracking algorithm identified a substantial fraction of mesocyclones (or storm objects) near the coast (i.e., from −20 to 0 km inland; Fig. 9b). The storm objects were distributed both over water and over land. A substantial portion of objects were identified between −10 and 0 km inland compared to the objects identified over water at the same ranges. Additionally, the storm objects (whether over water or over land) near the coast are noted to be more intense in this analysis (Fig. 9b), consistent with the findings of Baker et al. (2009), Green et al. (2011), and Alford et al. (2023b). However, the median values of AzShear onshore and offshore are nearly identical. Unlike Alford et al. (2023b), the storm objects here were tracked regardless of whether they produced a tornado or not.

Although the supercell mesocyclone median AzShear values are similar onshore and offshore (Fig. 9), it is the net change in mesocyclone intensity that is important to examine and to account for differences in mesocyclone intensity between storms. Thus, for each of the nine storms, we normalize the AzShear values at each time by the storm-lifetime-maximum AzShear. The method is identical to Alford et al. (2023b), who likewise normalized each storm by its lifetime mesocyclone maximum intensity. Figure 10a shows the distribution of normalized AzShear as a function of coast-relative distance. Unlike the results in Fig. 9b, there tend to be higher values of normalized AzShear onshore than offshore, suggesting that the supercell mesocyclones in Irene became more intense as they moved onshore. Indeed, the median value of normalized AzShear is higher onshore (0.79) than offshore (0.64). Likewise, we examine the distribution of normalized AzShear onshore and offshore in Fig. 10b. Both the median and the distribution of normalized AzShear increase in the onshore distribution. We found the differences in the onshore and offshore distributions to be statistically significant at the 95% confidence interval when using a two-sided Kolmogorov–Smirnov statistical test (Virtanen et al. 2020).

5. Discussion

a. Summary

This study has examined 1) the variability of kinematic supercell environments and 2) the intensity of low-level supercell mesocyclones within 30 km of the coastline in landfalling tropical cyclones. Using high-resolution dual-Doppler analyses collected by the SRs and nearby WSR-88Ds, the effects of the hurricane boundary layer transition (Alford et al. 2020) on the variability of VWS have been documented in observations in detail for the first time. Using coastal-composite wind profiles from spatiotemporally averaged dual-Doppler winds, the low-level wind speed was shown to reduce more than the winds above the boundary layer over land. As such, total VWS and SRH were shown to increase within the first 10–20 km inland, particularly when the background flow is more perpendicular to the coast. We then examined the effects of the changing structure of the TC flow by normalizing the VWS and SRH. We found that normalized VWS and SRH likewise increase inland. We also examined the BVWS relationship with total VWS and found that the BVWS primarily augmented the deep-layer (>8 km deep) total VWS. In the low levels where VWS is more likely to influence mesocyclone intensity, we found that the "TC-induced VWS" was of greater importance below 3 km in Irene, consistent with past findings (Schenkel et al. 2020, 2021). In contrast, BVWS was shown to be constructive through the entire depth of the Laura analyses. To examine how individual supercells respond to the coast, single-Doppler analyses were examined in Irene. In general, single-Doppler AzShear in individual supercells was found to increase as supercell mesocyclones crossed the coastal boundary. This finding is consistent with the recent work of (Alford et al. 2023b).

b. Relevance to past studies

Past studies of TC supercells have often focused on locations of tornadoes relative to TC motion (e.g., Gentry 1983), inner core versus outer rainbands (Weiss 1987), vertical wind shear (Schenkel et al. 2020), and coast-relative distance (Schultz and Cecil 2009; Schenkel et al. 2021). The primary motivation of this study was to understand why many tornadoes often occur within the first 50 km of the coastline. Various case studies have pointed to baroclinic boundaries along the coast due to synoptic fronts or contrasts between ocean and land thermodynamic profiles (Baker et al. 2009; Green et al. 2011). Others have pointed to convergence due to the decrease in the low-level wind along the coast (Gentry 1983; Green et al. 2011). The study by Green et al. (2011) is one example that shows a relatively narrow strip of convergent flow largely just off the coast in a simulation of Hurricane Katrina, albeit at 125-m altitude (i.e., below the observable level of most dual-Doppler analyses). In the coastal-composite profiles in Hurricanes Frances and Laura (Figs. 3c and 4c), there is evidence that near-coastal convergence is strongest below

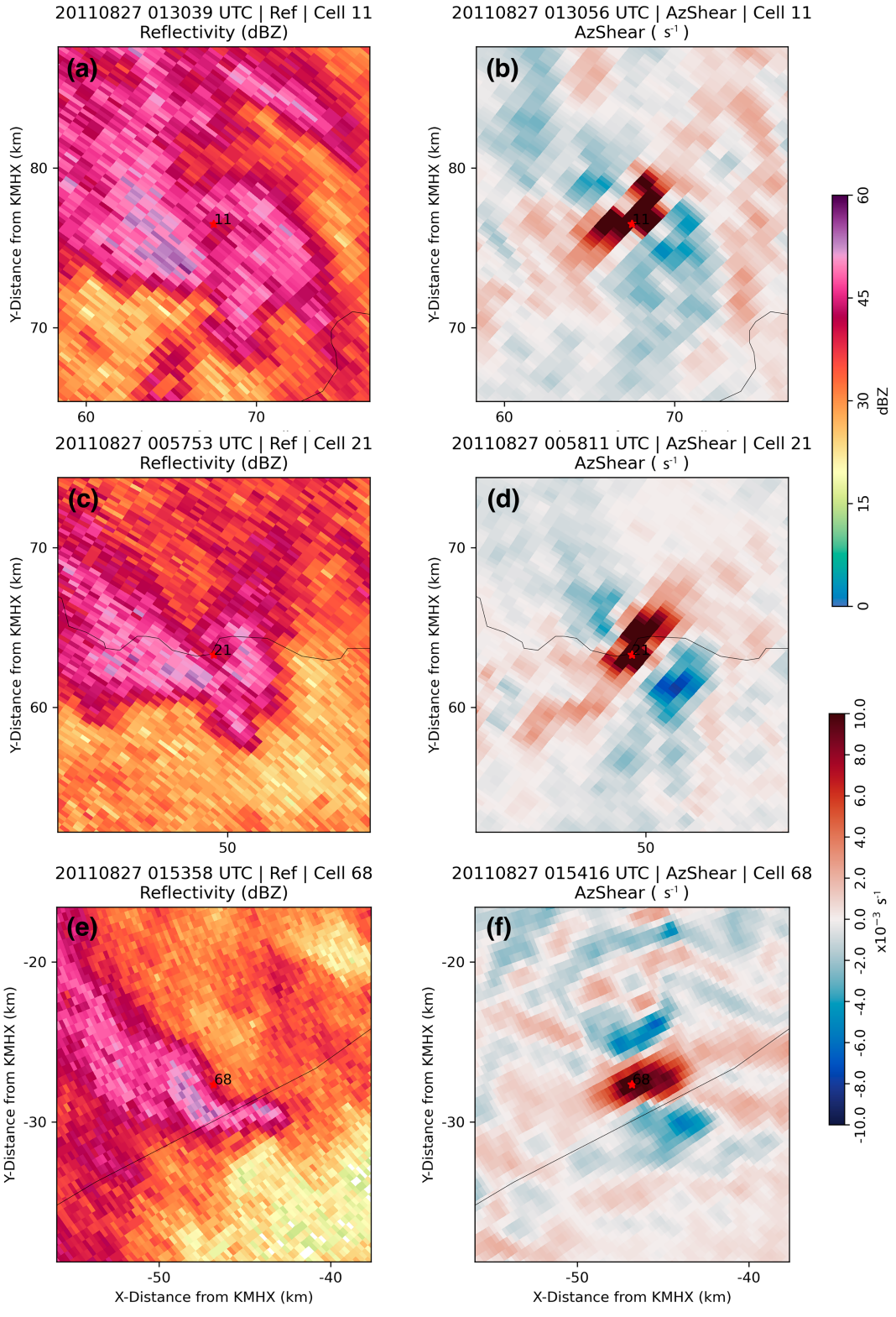

FIG. 8. Examples of supercells tracked in Hurricane Irene. Cells with the identification numbers (top) 11, (middle) 21, and (bottom) 68 are shown. (left) Radar reflectivity (dBZ). (right) AzShear (s^{-1}). The red star shows the location of the maximum AzShear.

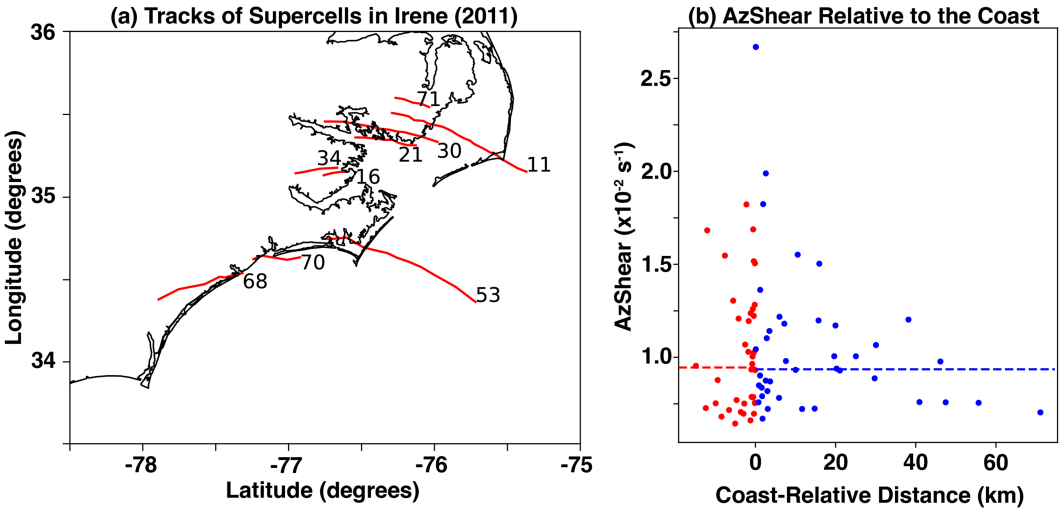

FIG. 9. (a) The tracks of supercells moving from ocean to land in Hurricane Irene. The cell number is shown near the beginning of each track. (b) A scatterplot of AzShear values from all storms in (a) is shown as a function of coast-relative distance (negative distance is inland). The AzShear points in (b) are separated by red (onshore) and blue (offshore) points for clarity. The median values of AzShear onshore and offshore are shown in the dashed red and blue lines, respectively.

1 km within 5 km of the coastline. In contrast in Hurricane Irene, general low-level divergence was found (Fig. 3c), but was related to the compositing of the divergence field across complex coastal waterways/coastal boundaries relative to the direction of the low-level flow. A zone of convergence offshore suggests that the wind field begins responding to the coast over the ocean, rather than at the ocean–land interface. Likewise, normalized VWS begins increasing over the ocean nearer the shore in both Irene and Laura (Fig. 6). The reason for increases may not be fully resolved by dual-Doppler analyses, as changes in sea surface aerodynamic surface roughness in increasingly shallow waters are not accounted for (e.g., Powell et al. 2003). Changes in individual supercell mesocyclone intensity were seen just offshore in this study (Fig. 10) and in Alford et al. (2023b). Hence, we suggest a gradual increase in aerodynamic surface roughness in shallow waters likely affects VWS, SRH, and convergence and should be examined in future studies.

We also discussed the results in the context of the coastal-compositing technique that largely yielded analyses along the internal boundary layer response in Frances and Irene versus across the internal boundary layer response in Laura. In Irene and Frances, clear differences in the total VWS over water versus over land were observed in VWS, which we attribute to the effects of the boundary layer transition across the coastal interface. In both Frances and Irene, the flow direction was more perpendicular to the coast than in Laura. In Laura, the flow (within the dual-Doppler domain) was more parallel to the coast and was representative of trajectories with relatively long histories over land. Near the coast in the analysis, an inland maximum in VWS/SRH is observed where trajectory histories over land were relatively shorter. The profiles with longer trajectories over land are indicative of wind profiles that had more completely adjusted to the inland surface roughness changes. As such, the contrast between total VWS and SRH over land is more muted in Laura. Nevertheless, the small increase in total VWS and SRH between −10 and 0 km inland in Laura is still likely the result of the over land boundary layer adjustment, but from trajectories upstream (i.e., southeast of the Laura dual-Doppler domain). These results are consistent with studies of internal boundary layer growth (e.g., Garratt 1990; Hirth et al. 2012). In addition to the general geometry of the coastline relative to the direction of the background flow, the complexity of the local coastline can affect VWS and SRH, as shown in the results of Frances. Multiple inland waterways were contained within the dual-Doppler domain of Frances, and individual maxima in VWS were observed as the flow crossed the waterways back onto land. The result is consistent with the work of Hirth et al. (2012), who likewise examined the internal boundary layer response and the complexity therein using the same dataset. However, a point only peripherally examined in this study is how the geometry and complexities of the coastline interface with the background shear (in addition to the distribution of buoyancy, which was not examined here), which is likely critical to sufficient supercell storm and by extension mesocyclone organization (Schenkel et al. 2020; Nowotarski et al. 2021; Paredes et al. 2021; Trier et al. 2023). Likewise, changes in the spatial structure, including changes in the vertical structure of the horizontal wind, of the TC wind field as a function of TC maximum intensity (Franklin et al. 2003; Zhang et al. 2011) relative to the geometry of the coast were not directly examined here. A more comprehensive study leveraging both kinematic and thermodynamic data should be performed in the future.

Regardless of tornado production in an individual TC, this study suggests that the evolution of the boundary layer structure results in an increase in VWS and SRH inland of the

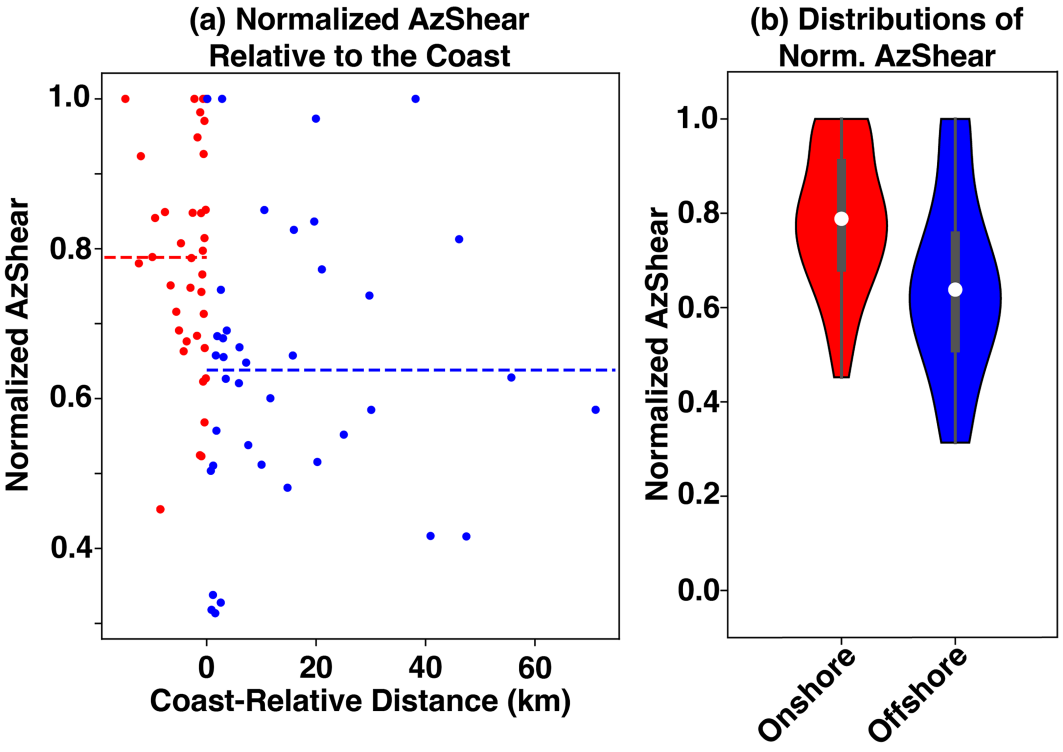

FIG. 10. (a) A scatterplot of normalized AzShear is shown as a function of coast-relative distance (negative distance is inland). The median values of normalized AzShear onshore and offshore distributions are shown in the red and blue dashed lines, respectively. (b) Violin plots of the normalized AzShear values offshore and onshore in red and blue, respectively. In the violin plots, the white dot represents the median of the distribution. The thick gray lines represent the inner-quartile range, the lower whisker shows the lowest datum above the first quartile minus the inner-quartile range, and the upper whisker denotes the highest datum above the first quartile plus the inner-quartile range.

coastal boundary, particularly when the flow is quasi perpendicular to the coastline. Morin and Parker (2011) indeed suggested such evolution was likely based on numerical modeling. Further evidence from observational works such as Hirth et al. (2012) and Alford et al. (2020 and 2023b) supported such a hypothesis, but did not directly examine VWS or SRH as a function of coast-relative distance. Therefore, this study confirms that VWS and SRH increase as the low-level wind field responds to the step function increase in surface roughness. They may also be affected by the magnitude of area-mean inland surface roughness. Further observational and/or numerical modeling studies should be undertaken to examine this hypothesis.

Finally, individual supercell responses to the more favorable VWS environment as storms move inland were examined. Alford et al. (2023b) examined tornadic mesocyclones crossing the coastal boundary and showed that storms often intensified quickly upon moving inland and some evidence for the increase in mesocyclone intensity beginning just offshore. In this study, we further examine mesocyclones in Irene regardless of tornado production. Similar to Alford et al. (2023b), we found that storms at times intensified as they moved across the coast. The single-Doppler results that included both tornadic and nontornadic mesocyclones largely mirrored the results of Alford et al. (2023b) and further suggest that individual storms do intensify as a result of their interaction with the changing kinematic environment at the coastal boundary. However, we did not examine storms that formed well inland of the coast and moved further inland. Previous climatologies (Pearson and Sadowski 1965; Schultz and Cecil 2009; Schenkel et al. 2021) suggest a minimum in tornadoes deeper inland relative to those produced very near the coast. Further work will be required to examine whether such a result is widely applicable.

c. *Relevance to operations and future work*

This study has examined the often undersampled environmental variability of TC supercell environments and the storm-scale responses of supercell mesocyclones. Both topics are important for forecasters at the NOAA Storm Prediction Center and National Weather Service, for example. While TC supercells continue to be difficult to sample from a radar perspective due to their shallow depths and small sizes (Spratt et al. 1997), the results of this study suggest that supercell or supercell-like structures should be carefully monitored, particularly as they move onshore during TC landfalls. To more completely characterize the evolution of supercells, particularly as they move quickly onshore, emerging technology such as phased array radar will afford rapid volumetric updates for kinematic and polarimetric variables and will be increasingly

critical for research and potentially operational settings as an option for replacing the WSR-88D system in the 2035–40 time frame (Palmer et al. 2022; Kollias et al. 2022).

While the national radiosonde network can characterize mesoalpha- to synoptic-scale environments, the results herein suggest that mesobeta-scale environments, which are often difficult to sample, are integral to the evolution of TC supercells. Results from MacDonald and Nowotarski (2023) indicate numerical models and mesoscale analysis products underpredict both buoyancy and VWS. The VWS bias may be augmented further near the coast based on the results of this manuscript and should be examined in future work. In addition, we note that this study focused on the storm-scale changes in mesocyclone intensity. While intensifying storms are generally expected to be more likely to produce tornadoes, we could not utilize the datasets here to directly examine tornadogenesis (or lack thereof) as supercells interact with the inland environment.

Acknowledgments. This work was supported by the NOAA/Office of Oceanic and Atmospheric Research under the NOAA-University of Oklahoma Cooperative Agreement NA21OAR4320204, U.S. Department of Commerce. S. H. was supported by the National Weather Center Research Experience for Undergraduates program funded by the National Science Foundation (AGS-1560419). A. A. was supported by the Peter Lamb Postdoctoral Fellowship (under NA21OAR4320204) as well as by the NOAA/OAR National Severe Storms Laboratory. B. S. was supported by NSF AGS-2028151 and the NOAA VORTEX-SE program. M. B. was supported by the National Institute for Standards and Technology (70NANB19H056), which also supported the SR deployment in Hurricane Laura. We thank Dr. Tom Galarneau and Dr. Larry Hopper (NOAA/OAR NSSL) for their helpful comments that improved this manuscript. We thank three anonymous reviewers for their comments that improved this manuscript.

Data availability statement. The dual-Doppler data in Hurricane Irene may be found at https://doi.org/10.5281/zenodo.3494891. The ground-based radar data from Hurricanes Laura and Frances and the supercell track data in Irene may be accessed at https://doi.org/10.5281/zenodo.11584504.

REFERENCES

Alford, A. A., M. I. Biggerstaff, and G. D. Carrie, 2019a: Mobile ground-based SMART radar observations and wind retrievals during the landfall of Hurricane Harvey (2017). *Geosci. Data J.*, **6**, 205–213, https://doi.org/10.1002/gdj3.82.

——, ——, ——, J. L. Schroeder, B. D. Hirth, and S. M. Waugh, 2019b: Near-surface maximum winds during the landfall of Hurricane Harvey. *Geophys. Res. Lett.*, **46**, 973–982, https://doi.org/10.1029/2018GL080013.

——, J. A. Zhang, M. I. Biggerstaff, P. Dodge, F. D. Marks, and D. J. Bodine, 2020: Transition of the hurricane boundary layer during the landfall of Hurricane Irene (2011). *J. Atmos. Sci.*, **77**, 3509–3531, https://doi.org/10.1175/jas-d-19-0290.1.

——, M. I. Biggerstaff, C. L. Ziegler, D. P. Jorgensen, and G. D. Carrie, 2022: A method for correcting staggered pulse repetition time (PRT) and dual pulse repetition frequency (PRF) processor errors in research radar datasets. *J. Atmos. Oceanic Technol.*, **39**, 1763–1780, https://doi.org/10.1175/JTECH-D-21-0176.1.

——, ——, and G. Carrie, 2023a: Using ground-based radar observations to evaluate asymmetric convection and eyewall dynamics during the landfall of Hurricane Harvey (2017). *J. Atmos. Sci.*, **80**, 1867–1889, https://doi.org/10.1175/JAS-D-22-0053.1.

——, A. Messersmith, B. Pollock, Q. Thomas, T. N. Sandmæl, and B. A. Schenkel, 2023b: Tropical cyclone supercell response to the coast using a climatology of radar-derived azimuthal shear. *Geophys. Res. Lett.*, **50**, e2023GL105977, https://doi.org/10.1029/2023gl105977.

Baker, A. K., M. D. Parker, and M. D. Eastin, 2009: Environmental ingredients for supercells and tornadoes within Hurricane Ivan. *Wea. Forecasting*, **24**, 223–244, https://doi.org/10.1175/2008WAF2222146.1.

Bell, M. M., and W.-C. Lee, 2012: Objective tropical cyclone center tracking using single-Doppler radar. *J. Appl. Meteor. Climatol.*, **51**, 878–896, https://doi.org/10.1175/JAMC-D-11-0167.1.

Betten, D. P., M. I. Biggerstaff, and C. L. Ziegler, 2018: Three-dimensional storm structure and low-level boundaries at different stages of cyclic mesocyclone evolution in a high-precipitation tornadic supercell. *Adv. Meteor.*, **2018**, 24, https://doi.org/10.1155/2018/9432670.

Biggerstaff, M. I., and R. A. Houze Jr., 1991: Midlevel vorticity structure of the 10–11 June 1985 squall line. *Mon. Wea. Rev.*, **119**, 3066–3079, https://doi.org/10.1175/1520-0493(1991)119<3066:MVSOTJ>2.0.CO;2.

——, and Coauthors, 2005: The shared mobile atmospheric research and teaching radar: A collaboration to enhance research and teaching. *Bull. Amer. Meteor. Soc.*, **86**, 1263–1274, https://doi.org/10.1175/BAMS-86-9-1263.

——, J. A. Stevenson, A. A. Alford, and G. D. Carrie, 2021: Hurricane Florence (2018): Long duration single- and dual-Doppler observations and wind retrievals during landfall. *Geosci. Data J.*, **9**, 273–287, https://doi.org/10.1002/gdj3.137.

Bogner, P. B., G. M. Barnes, and J. L. Franklin, 2000: Conditional instability and shear for six hurricanes over the Atlantic Ocean. *Wea. Forecasting*, **15**, 192–207, https://doi.org/10.1175/1520-0434(2000)015<0192:CIASFS>2.0.CO;2.

Brauer, N. S., J. B. Basara, C. R. Homeyer, G. M. McFarquhar, and P. E. Kirstetter, 2020: Quantifying precipitation efficiency and drivers of excessive precipitation in post-landfall Hurricane Harvey. *J. Hydrometeor.*, **21**, 433–452, https://doi.org/10.1175/JHM-D-19-0192.1.

Bunkers, M. J., B. A. Klimowski, J. W. Zeitler, R. L. Thompson, and M. L. Weisman, 2000: Predicting supercell motion using a new hodograph technique. *Wea. Forecasting*, **15**, 61–79, https://doi.org/10.1175/1520-0434(2000)015<0061:PSMUAN>2.0.CO;2.

Carroll-Smith, D. L., L. C. Dawson, and R. J. Trapp, 2019: High-resolution real-data WRF modeling and verification of tropical cyclone tornadoes associated with Hurricane Ivan (2004). *Electron. J. Severe Storms Meteor.*, **14** (2), https://ejssm.com/ojs/index.php/site/article/view/72.

Chen, J., and D. R. Chavas, 2020: The transient responses of an axisymmetric tropical cyclone to instantaneous surface roughening and drying. *J. Atmos. Sci.*, **77**, 2807–2834, https://doi.org/10.1175/JAS-D-19-0320.1.

Coffer, B. E., M. D. Parker, R. L. Thompson, B. T. Smith, and R. E. Jewell, 2019: Using near-ground storm relative helicity in supercell tornado forecasting. *Wea. Forecasting*, **34**, 1417–1435, https://doi.org/10.1175/WAF-D-19-0115.1.

Curtis, L., 2004: Midlevel dry intrusions as a factor in tornado outbreaks associated with landfalling tropical cyclones from the Atlantic and Gulf of Mexico. *Wea. Forecasting*, **19**, 411–427, https://doi.org/10.1175/1520-0434(2004)019<0411:MDIAAF>2.0.CO;2.

Davies-Jones, R., 1984: Streamwise vorticity: The origin of updraft rotation in supercell storms. *J. Atmos. Sci.*, **41**, 2991–3006, https://doi.org/10.1175/1520-0469(1984)041<2991:SVTOOU>2.0.CO;2.

Davis, C., C. Snyder, and A. C. Didlake Jr., 2008: A vortex-based perspective of eastern Pacific tropical cyclone formation. *Mon. Wea. Rev.*, **136**, 2461–2477, https://doi.org/10.1175/2007MWR2317.1.

del Moral, A., T. M. Weckwerth, T. Rigo, M. M. Bell, and M. C. Llasat, 2020: C-band dual-Doppler retrievals in complex terrain: Improving the knowledge of severe storm dynamics in Catalonia. *Remote Sens.*, **12**, 2930, https://doi.org/10.3390/rs12182930.

Devanas, A., D. Gregoria, K. Kasper, and P. Santos, 2008: Tropical cyclone induced tornadoes associated with the formation of Tropical Storm Barry. *20th Conf. on Climate Variability and Change*, New Orleans, LA, Amer. Meteor. Soc., JP3.16, https://ams.confex.com/ams/88Annual/techprogram/paper_131758.htm.

DiGangi, E. A., D. R. MacGorman, C. L. Ziegler, D. Betten, M. Biggerstaff, M. Bowlan, and C. K. Potvin, 2016: An overview of the 29 May 2012 Kingfisher supercell during DC3. *J. Geophys. Res. Atmos.*, **121**, 14 316–14 343, https://doi.org/10.1002/2016JD025690.

Doviak, R. J., P. S. Ray, R. G. Strauch, and L. J. Miller, 1976: Error estimation in wind fields derived from dual-Doppler radar measurement. *J. Appl. Meteor.*, **15**, 868–878, https://doi.org/10.1175/1520-0450(1976)015<0868:EEIWFD>2.0.CO;2.

Eastin, M. D., and M. C. Link, 2009: Miniature supercells in an offshore outer rainband of Hurricane Ivan (2004). *Mon. Wea. Rev.*, **137**, 2081–2104, https://doi.org/10.1175/2009MWR2753.1.

——, T. L. Gardner, M. C. Link, and K. C. Smith, 2012: Surface cold pools in the outer rainbands of Tropical Storm Hanna (2008) near landfall. *Mon. Wea. Rev.*, **140**, 471–491, https://doi.org/10.1175/MWR-D-11-00099.1.

Edwards, R., 2012: Tropical cyclone tornadoes: A review of knowledge in research and prediction. *Electron. J. Severe Storms Meteor.*, **7**, 1–61, https://ejssm.com/ojs/index.php/site/article/view/42.

——, and A. Pietrycha, 2006: Archetypes for surface baroclinic boundaries influencing tropical cyclone tornado occurrence. *23rd Conf. on Severe Local Storms*, St. Louis, MO, Amer. Meteor. Soc., P8.2, https://ams.confex.com/ams/23SLS/techprogram/paper_114992.htm.

——, and R. L. Thompson, 2012: Reversible CAPE in tropical cyclone tornado regimes. *Proc. 27th Conf. on Severe Local Storms*, Madison, WI, Amer. Meteor. Soc., 88, https://ams.confex.com/ams/27SLS/webprogram/Paper254328.html.

——, and R. M. Mosier, 2022: Over a quarter century of TCTOR: Tropical cyclone tornadoes in the WSR-88D era. *Proc. 30th Conf. on Severe Local Storms*, Santa Fe, NM, Amer. Meteor. Soc., 171, https://ams.confex.com/ams/30SLS/meetingapp.cgi/Paper/407018.

——, A. R. Dean, R. L. Thompson, and B. T. Smith, 2012: Convective modes for significant severe thunderstorms in the contiguous United States. Part III: Tropical cyclone tornadoes. *Wea. Forecasting*, **27**, 1507–1519, https://doi.org/10.1175/WAF-D-11-00117.1.

Fernández-Cabán, P. L., and Coauthors, 2019: Observing Hurricane Harvey's eyewall at landfall. *Bull. Amer. Meteor. Soc.*, **100**, 759–775, https://doi.org/10.1175/BAMS-D-17-0237.1.

Franklin, J. L., M. L. Black, and K. Valde, 2003: GPS dropwindsonde wind profiles in hurricanes and their operational implications. *Wea. Forecasting*, **18**, 32–44, https://doi.org/10.1175/1520-0434(2003)018<0032:GDWPIH>2.0.CO;2.

Galarneau, T. J., Jr., and C. A. Davis, 2013: Diagnosing forecast errors in tropical cyclone motion. *Mon. Wea. Rev.*, **141**, 405–430, https://doi.org/10.1175/MWR-D-12-00071.1.

Garratt, J. R., 1990: The internal boundary layer—A review. *Bound.-Layer Meteor.*, **50**, 171–203, https://doi.org/10.1007/BF00120524.

Gentry, R. C., 1983: Genesis of tornadoes associated with hurricanes. *Mon. Wea. Rev.*, **111**, 1793–1805, https://doi.org/10.1175/1520-0493(1983)111<1793:GOTAWH>2.0.CO;2.

Green, B. W., F. Zhang, and P. Markowski, 2011: Multiscale processes leading to supercells in the landfalling outer rainbands of Hurricane Katrina (2005). *Wea. Forecasting*, **26**, 828–847, https://doi.org/10.1175/WAF-D-10-05049.1.

Helmus, J. J., and S. M. Collis, 2016: The Python ARM Radar Toolkit (Py-ART), a library for working with weather radar data in the Python programming language. *J. Open Res. Software*, **4**, e25, https://doi.org/10.5334/jors.119.

Hersbach, H., and Coauthors, 2020: The ERA5 global reanalysis. *Quart. J. Roy. Meteor. Soc.*, **146**, 1999–2049, https://doi.org/10.1002/qj.3803.

Hirth, B. D., J. L. Schroeder, C. C. Weiss, D. A. Smith, and M. I. Biggerstaff, 2012: Research radar analyses of the internal boundary layer over Cape Canaveral, Florida, during the landfall of Hurricane Frances (2004). *Wea. Forecasting*, **27**, 1349–1372, https://doi.org/10.1175/WAF-D-12-00014.1.

Hlywiak, J., and D. S. Nolan, 2021: The response of the near-surface tropical cyclone wind field to inland surface roughness length and soil moisture content during and after landfall. *J. Atmos. Sci.*, **78**, 983–1000, https://doi.org/10.1175/JAS-D-20-0211.1.

Knapp, K. R., M. C. Kruk, D. H. Levinson, H. J. Diamond, and C. J. Neumann, 2010: The International Best Track Archive for Climate Stewardship (IBTrACS): Unifying tropical cyclone data. *Bull. Amer. Meteor. Soc.*, **91**, 363–376, https://doi.org/10.1175/2009BAMS2755.1.

Knupp, K. R., J. Walters, and M. Biggerstaff, 2006: Doppler profiler and radar observations of boundary layer variability during the landfall of Tropical Storm Gabrielle. *J. Atmos. Sci.*, **63**, 234–251, https://doi.org/10.1175/JAS3608.1.

Kollias, P., and Coauthors, 2022: Science applications of phased array radars. *Bull. Amer. Meteor. Soc.*, **103**, E2370–E2390, https://doi.org/10.1175/BAMS-D-21-0173.1.

Kosiba, K. A., and J. Wurman, 2014: Finescale dual-Doppler analysis of hurricane boundary layer structures in Hurricane Frances (2004) at landfall. *Mon. Wea. Rev.*, **142**, 1874–1891, https://doi.org/10.1175/MWR-D-13-00178.1.

MacDonald, L. M., and C. J. Nowotarski, 2023: Verification of Rapid Refresh and High-Resolution Rapid Refresh model variables in tornadic tropical cyclones. *Wea. Forecasting*, **38**, 655–675, https://doi.org/10.1175/WAF-D-22-0117.1.

Mahalik, M. C., B. R. Smith, K. L. Elmore, D. M. Kingfield, K. L. Ortega, and T. M. Smith, 2019: Estimates of gradients in radar moments using a linear least squares derivative technique. *Wea. Forecasting*, **34**, 415–434, https://doi.org/10.1175/WAF-D-18-0095.1.

Martinaitis, S. M., 2017: Radar observations of tornado-warned convection associated with tropical cyclones over Florida. *Wea. Forecasting*, **32**, 165–186, https://doi.org/10.1175/WAF-D-16-0105.1.

McCaul, E. W., Jr., 1991: Buoyancy and shear characteristics of hurricane-tornado environments. *Mon. Wea. Rev.*, **119**, 1954–1978, https://doi.org/10.1175/1520-0493(1991)119<1954:BASCOH>2.0.CO;2.

——, and M. L. Weisman, 1996: Simulations of shallow supercell storms in landfalling hurricane environments. *Mon. Wea. Rev.*, **124**, 408–429, https://doi.org/10.1175/1520-0493(1996)124<0408:SOSSSI>2.0.CO;2.

——, and ——, 2001: The sensitivity of simulated supercell structure and intensity to variations in the shapes of environmental buoyancy and shear profiles. *Mon. Wea. Rev.*, **129**, 664–687, https://doi.org/10.1175/1520-0493(2001)129<0664:TSOSSS>2.0.CO;2.

——, D. E. Buechler, S. J. Goodman, and M. Cammarata, 2004: Doppler radar and lightning network observations of a severe outbreak of tropical cyclone tornadoes. *Mon. Wea. Rev.*, **132**, 1747–1763, https://doi.org/10.1175/1520-0493(2004)132<1747:DRALNO>2.0.CO;2.

Miller, R. L., C. L. Ziegler, and M. I. Biggerstaff, 2020: Seven-Doppler radar and in situ analysis of the 25–26 June 2015 Kansas MCS during PECAN. *Mon. Wea. Rev.*, **148**, 211–240, https://doi.org/10.1175/MWR-D-19-0151.1.

Molinari, J., and D. Vollaro, 2010: Distribution of helicity, CAPE, and shear in tropical cyclones. *J. Atmos. Sci.*, **67**, 274–284, https://doi.org/10.1175/2009JAS3090.1.

Morin, M. J., and M. D. Parker, 2011: A numerical investigation of supercells in landfalling tropical cyclones. *Geophys. Res. Lett.*, **38**, L10801, https://doi.org/10.1029/2011GL047448.

Novlan, D. J., and W. M. Gray, 1974: Hurricane-spawned tornadoes. *Mon. Wea. Rev.*, **102**, 476–488, https://doi.org/10.1175/1520-0493(1974)102<0476:HST>2.0.CO;2.

Nowotarski, C. J., and P. M. Markowski, 2016: Modifications to the near-storm environment induced by simulated supercell thunderstorms. *Mon. Wea. Rev.*, **144**, 273–293, https://doi.org/10.1175/MWR-D-15-0247.1.

——, J. Spotts, R. Edwards, S. Overpeck, and G. R. Woodall, 2021: Tornadoes in Hurricane Harvey. *Wea. Forecasting*, **36**, 1589–1609, https://doi.org/10.1175/WAF-D-20-0196.1.

Oye, R. C., C. Mueller, and S. Smith, 1995: Software for radar translation, visualization, editing, and interpolation. *27th Conf. on Radar Meteorology*, Vail, CO, Amer. Meteor. Soc., 359–361.

Palmer, R., and Coauthors, 2022: A primer on phased array radar technology for the atmospheric sciences. *Bull. Amer. Meteor. Soc.*, **103**, E2391–E2416, https://doi.org/10.1175/BAMS-D-21-0172.1.

Paredes, M., B. A. Schenkel, R. Edwards, and M. Coniglio, 2021: Tropical cyclone outer size impacts the number and location of tornadoes. *Geophys. Res. Lett.*, **48**, e2021GL095922, https://doi.org/10.1029/2021GL095922.

Parker, M. D., 2014: Composite VORTEX2 supercell environments from near-storm soundings. *Mon. Wea. Rev.*, **142**, 508–529, https://doi.org/10.1175/MWR-D-13-00167.1.

Pasch, R., R. Berg, D. R. Roberts, and P. P. Papin, 2020: Tropical cyclone report: Hurricane Laura (AL132020), 20–29 August 2020. NHC Tech. Rep., 75 pp., https://www.nhc.noaa.gov/data/tcr/AL132020_Laura.pdf.

Pearson, A. D., and A. F. Sadowski, 1965: Hurricane-induced tornadoes and their distribution. *Mon. Wea. Rev.*, **93**, 461–464, https://doi.org/10.1175/1520-0493(1965)093<0461:HITATD>2.3.CO;2.

Potvin, C. K., D. Betten, L. J. Wicker, K. L. Elmore, and M. I. Biggerstaff, 2012: 3DVAR vs. traditional dual-Doppler wind retrievals of a simulated supercell thunderstorm. *Mon. Wea. Rev.*, **140**, 3487–3494, https://doi.org/10.1175/MWR-D-12-00063.1.

Powell, M. D., P. J. Vickery, and T. A. Reinhold, 2003: Reduced drag coefficient for high wind speeds in tropical cyclones. *Nature*, **422**, 279–283, https://doi.org/10.1038/nature01481.

Ramsay, H. A., and C. A. Doswell III, 2005: A sensitivity study of hodograph-based methods for estimating supercell motion. *Wea. Forecasting*, **20**, 954–970, https://doi.org/10.1175/WAF889.1.

Rappaport, E. N., 2014: Fatalities in the United States from Atlantic tropical cyclones: New data and interpretation. *Bull. Amer. Meteor. Soc.*, **95**, 341–346, https://doi.org/10.1175/BAMS-D-12-00074.1.

Sandmæl, T. N., and Coauthors, 2023: The tornado probability algorithm: A probabilistic machine learning tornadic circulation detection algorithm. *Wea. Forecasting*, **38**, 445–466, https://doi.org/10.1175/WAF-D-22-0123.1.

Schenkel, B. A., R. Edwards, and M. Coniglio, 2020: A climatological analysis of ambient deep-tropospheric vertical wind shear impacts upon tornadoes in tropical cyclones. *Wea. Forecasting*, **35**, 2033–2059, https://doi.org/10.1175/WAF-D-19-0220.1.

——, M. Coniglio, and R. Edwards, 2021: How does the relationship between ambient deep-tropospheric vertical wind shear and tropical cyclone tornadoes change between coastal and inland environments? *Wea. Forecasting*, **36**, 539–566, https://doi.org/10.1175/WAF-D-20-0127.1.

——, K. M. Calhoun, T. N. Sandmæl, Z. R. Fruits, I. Schick, M. C. Ake, and B. F. Kassel, 2023: Lightning and radar characteristics of tornadoes in landfalling tropical cyclones. *J. Geophys. Res. Atmos.*, **128**, e2023JD038685, https://doi.org/10.1029/2023JD038685.

Schultz, L. A., and D. J. Cecil, 2009: Tropical cyclone tornadoes, 1950-2007. *Mon. Wea. Rev.*, **137**, 3471–3484, https://doi.org/10.1175/2009MWR2896.1.

Shapiro, A., K. M. Willingham, and C. K. Potvin, 2010: Spatially variable advection correction of radar data. Part I: Theoretical considerations. *J. Atmos. Sci.*, **67**, 3445–3456, https://doi.org/10.1175/2010JAS3465.1.

Sibson, R., 1981: A brief description of natural neighbor interpolation. *Interpreting Multivariate Data*, V. Barnett, Ed., John Wiley, 21–36.

Spratt, S. M., D. W. Sharp, P. Welsh, A. Sandrik, F. Alsheimer, and C. Paxton, 1997: A WSR-88D assessment of tropical cyclone outer rainband tornadoes. *Wea. Forecasting*, **12**, 479–501, https://doi.org/10.1175/1520-0434(1997)012<0479:AWAOTC>2.0.CO;2.

Trier, S. B., D. A. Ahijevych, D. Carroll-Smith, G. H. Bryan, and R. Edwards, 2023: Composite mesoscale environmental conditions influencing tornado frequencies in landfalling tropical cyclones. *Wea. Forecasting*, **38**, 2481–2508, https://doi.org/10.1175/WAF-D-22-0227.1.

Vescio, M. D., S. J. Weiss, and F. P. Ostby, 1996: Tornadoes associated with Tropical Storm Beryl. *Natl. Wea. Dig.*, **21**, 2–10.

Virtanen, P., and Coauthors, 2020: SciPy 1.0: Fundamental algorithms for scientific computing in Python. *Nat. Methods*, **17**, 261–272, https://doi.org/10.1038/s41592-019-0686-2.

Wade, A. R., M. C. Coniglio, and C. L. Ziegler, 2018: Comparison of near- and far-field supercell inflow environments using radiosonde observations. *Mon. Wea. Rev.*, **146**, 2403–2415, https://doi.org/10.1175/MWR-D-17-0276.1.

Weiss, S. J., 1987: Some climatological aspects of forecasting tornadoes associated with tropical cyclones. Preprints, *17th Conf. Hurricanes and Tropical Meteorology*, Miami, FL, Amer. Meteor. Soc., 160–163.

Wessel, P., and W. H. F. Smith, 1996: A global, self-consistent, hierarchical, high-resolution shoreline database. *J. Geophys. Res.*, **101**, 8741–8743, https://doi.org/10.1029/96JB00104.

Wingo, S. M., and K. R. Knupp, 2016: Kinematic structure of mesovortices in the eyewall of Hurricane Ike (2008) derived from ground-based dual-Doppler analysis. *Mon. Wea. Rev.*, **144**, 4245–4263, https://doi.org/10.1175/MWR-D-16-0085.1.

Wurman, J., Y. Richardson, C. Alexander, S. Weygandt, and P. F. Zhang, 2007: Dual-Doppler analysis of winds and vorticity budget terms near a tornado. *Mon. Wea. Rev.*, **135**, 2392–2405, https://doi.org/10.1175/MWR3404.1.

Yuter, S. E., and R. A. Houze Jr., 1995: Three-dimensional kinematic and microphysical evolution of Florida cumulonimbus. Part II: Frequency distributions of vertical velocity, reflectivity, and differential reflectivity. *Mon. Wea. Rev.*, **123**, 1941–1963, https://doi.org/10.1175/1520-0493(1995)123<1941:TDKAME>2.0.CO;2.

Zhang, J. A., R. F. Rogers, D. S. Nolan, and F. D. Marks Jr., 2011: On the characteristic height scales of the hurricane boundary layer. *Mon. Wea. Rev.*, **139**, 2523–2535, https://doi.org/10.1175/MWR-D-10-05017.1.